Characterizing the Temporal Dynamics of ^{129}Xe Spectroscopy to Uncover the Origins of Gas Exchange Impairment

by

Elianna A. Bier

Medical Physics Graduate Program
Duke University

Date:_______________________
Approved:

____
Bastiaan Driehuys, Supervisor

____
Sudarshan Rajagopal

____
Trong-Kha Truong

Thesis submitted in partial fulfillment of
the requirements for the degree of
Master of Science in the
Medical Physics Graduate Program
in the Graduate School of
Duke University

2017

ABSTRACT

Characterizing the Temporal Dynamics of ^{129}Xe Spectroscopy to Uncover the Origins of

Gas Exchange Impairment

by

Elianna A. Bier

Medical Physics Graduate Program
Duke University

Date:_______________________
Approved:

____
Bastiaan Driehuys, Supervisor

____
Sudarshan Rajagopal

____
Trong-Kha Truong

An abstract of a thesis submitted in partial fulfillment of
the requirements for the degree of
Master of Science in the
Medical Physics Graduate Program
in the Graduate School of
Duke University

2017

Abstract

^{129}Xe MRI has emerged as a promising means of imaging ventilation distribution. Recently, interest has turned from only imaging ventilation to exploring solubility and chemical shifts to characterize gas exchange, including images of gas exchange patterns that are sensitive to a wide array of disease. The next challenge is to differentiate the underlying causes of gas exchange impairment to begin enabling not just detection, but diagnosis. This prompted us to investigate the relatively unexplored dynamics of ^{129}Xe spectroscopy.

Hyperpolarized ^{129}Xe is a powerful noninvasive tool for studying the physiological environment of the lung due to its distinct chemical shifts as xenon diffuses from the airspaces, through the alveolar membrane, and into red blood cells (RBCs). Previous work has shown that the spectral characteristics (amplitude, chemical shift, line width, and phase) of each resonance are sensitive to disease. In principle, the dynamic variations in four spectral parameters of each ^{129}Xe resonance detected over inhalation, breath hold, and cardiac cycle can contain vital information on the origins of reduced lung function. In this work, our objective was to a) develop a framework for evaluating dynamics, b) assess temporal differences in spectroscopic parameters between patients with idiopathic pulmonary fibrosis (IPF) and healthy volunteers, c)

understand the interplay between lineshape and dynamics, and d) create metrics to test the sensitivity of dynamic spectroscopy to underlying lineshapes and signal to noise.

The developed analysis methods were used to characterize the spectral dynamics of 14 healthy volunteers and 10 subjects with IPF. In all subjects, the breathing maneuver (inhale, breath hold, exhale) was reflected in the chemical shift and line width of the ^{129}Xe RBC, barrier, and gas resonances. When comparing a representative IPF and healthy subject, we found that the subject with IPF had an RBC chemical shift that was initially 2 ppm lower and decreased by 0.5 ppm throughout a 5 s breath hold. Over the breath hold, we observed oscillations at the cardiac pulsation frequency in all of the spectral parameters of the RBC resonance. A mean peak-to-peak change of 7.9% ± 2.8% in amplitude of the RBC resonance was consistent across both cohorts. However, the oscillations in the chemical shift and phase of subjects with IPF were three times higher than in healthy volunteers. In light of the known relationship between RBC chemical shift and blood oxygenation levels, these findings suggest that we are sensitive to pathologically driven changes in blood oxygenation on the timescale of the cardiac cycle.

To analyze the effects of our spectral analysis in comparison to a known spectral model, we developed a digital dynamic spectroscopy phantom that simulated clinical free induction decays (FIDs) similar to what we collect during a dynamic spectroscopy acquisition based on specified spectral parameters. This phantom was used to validate our analysis techniques and explore the dependence of RBC signal oscillations on spectral structure. Additionally, motivated by a recent report that dissolved-phase xenon spectra is best fit to three dissolved-phase peaks, we performed a lineshape analysis on stationary spectra from a data set with higher spectral resolution. It was concluded that fitting to non-Lorentzian line shapes reduced the residual error of the fit and that the barrier resonance can potentially be represented by a linear combination of two Lorentzians where the spectral characteristics of the second peak are completely dependent on the first.

^{129}Xe dynamic spectroscopy can be used to evaluate the temporal variations in gas exchange, although additional work must be done to properly characterize the spectral structure. The derived dynamic metrics have the potential to be useful biomarkers for disease progression and help discriminate between different pathologies that affect gas exchange.

Contents

List of Tables

List of Figures

Acknowledgements

Bastiaan Driehuys

Scott Robertson

Geoff Schrank

Ziyi Wang

Mu He

Rohan Virgincar

Jennifer Wang

1 Motivation

Lung disease is the 3rd leading cause of death in the US [1], yet diagnostic tests are invasive or non-specific. Certain diseases, such as simple forms of asthma or chronic pulmonary obstructive disease (COPD) can be easily diagnosed with rudimentary pulmonary function test (PFTs) and clinical history. However, the diagnosis of interstitial lung disease (ILD), pulmonary vascular disease (PVD), or the workup of dyspnea (shortness of breath) in the setting of normal PFTs can be very challenging and require invasive biopsy or catheterization. Moreover, asthma and COPD are now recognized to consist of many different phenotypes caused by underlying conditions that cannot be teased apart by PFTs [2, 3]. After diagnosis, assessing disease progression is difficult because while PFTs offer a global assessment of lung function, they are exertion dependent, noisy, insensitive, and unable to detect the heterogeneous distribution of disease. Additionally, often these objective measures do not agree with patient reported symptoms. Diagnosis, phenotyping, and monitoring disease progression and response to therapy would greatly benefit from a method of probing the physiological cause of reduced gas exchange.

Current widespread imaging techniques are unable to directly image gas exchange. High-resolution computed tomography (HRCT) can aid in disease diagnosis, however it can only assess structural changes and abnormalities, all functional information must be inferred though structure-function relationships [4]. Furthermore, repeat CT scans carry increasing risks of radiation exposure limiting their use for monitoring disease progression and response [5]. Another imaging technique is a ventilation/perfusion (V/Q) scan, which use a radioactive nuclide to examine the relationship between two of the essential functions for gas exchange [6, 7]. When the V/Q ratio deviates from unity, it indicates abnormalities in lung function [8]. However, V/Q scans have low SNR, spatial resolution, temporal resolution, and heterogeneity in local V/Q ratios is observed even in healthy lungs. V/Q scans also expose the patient to a non-negligible radiation dose and cannot be used for longitudinal studies.

Recently, studies have shown that a hyperpolarized ^{129}Xe gas can be used as a contrast agent in MRI. Upon inhalation, the gas follows the functional pathway of oxygen as it diffuses from the alveoli through the alveolar membrane, pulmonary barrier tissues, and plasma, and finally into capillary red blood cells (RBCs). As the ^{129}Xe atoms dissolves into the barrier tissues and RBCs it exhibits different resonance frequency shifts [9, 10], that enable the uptake of each compartment to be imaged separately (Figure 1). Ventilation and gas exchange imaging is beginning to show exquisite sensitivity to a range of pulmonary pathologies, including ILD and PVD [11]. Still, despite this sensitivity to disease burden, ^{129}Xe imaging techniques are not able to distinguish many pulmonary diseases.

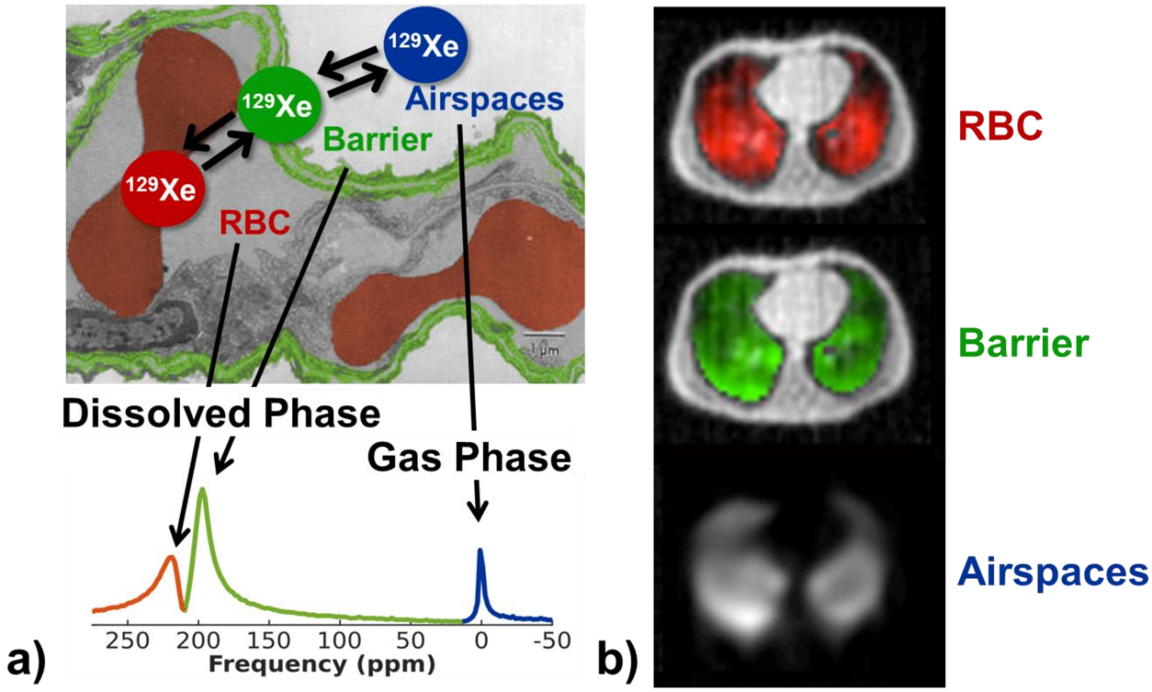

Figure 1. (a) Diagram of gas-phase ^{129}Xe transfer from the airspaces into the interstitial barrier tissues and capillary RBCs and the corresponding ^{129}Xe spectral peaks. (b) Images of ^{129}Xe in the RBC, barrier tissues and lung airspaces. ***Figure adapted from Robertson ISMRM 2016 [12] and Kaushik MRM 2016 [13].***

While gas exchange imaging is rooted in the ^{129}Xe spectroscopic features that permit the separation of the 3 compartments, such imaging sacrifices the ability to measure other spectroscopic details that contain vital information about the local physiological environment. The benefit of ^{129}Xe spectroscopy is that each spectral peak is not only characterized by amplitude, but also chemical shift, line width, and phase. These parameters provide yet another way to probe disease and provide insight on the underlying cause of reduced gas exchanges.

Gas exchange is an inherently dynamic process, with disease disrupting intrinsic time scales. Traditional spectroscopic analysis techniques average together many FIDs to improve the signal-to-noise ratio (SNR), removing all temporal information, and reducing lung function to a single static measurement. Instead, if ^{129}Xe spectra are measured as a function of time, they have the potential to help pinpoint the physiological causes of reduced lung function.

Ideally, ^{129}Xe dynamic spectroscopy would be used alongside ^{129}Xe imaging to aid in the diagnosis and monitoring of pulmonary disease. The goal of this research is to set up the analysis framework to characterize the temporal dynamics of spectroscopic parameters and understand the dependence of this analysis on the underlying spectral structure. This framework is also used to examine a relevant disease state to begin identifying the most promising dynamic spectroscopic markers of disease.

2 Relevant Theory

2.1 Physics

2.1.1 NMR Signal

The detection of ^{129}Xe signal is rooted in nuclear magnetic resonance. The origin of this is the bulk magnetization of nuclei arising from the alignment of individual nuclear magnetic moments to an external magnetic field. A nucleus has a magnetic moment only if it has an odd number of protons and/or neutrons, and thus only specific nuclei are NMR-active. The unpaired nucleons contribute a specific form of angular momentum termed spin, m, generating a magnetic dipole moment. The strength of the magnetic moment is directly proportional to the angular moment, J, and the gyromagnetic ratio, γ, of the nucleus.

$$\mu \equiv \gamma J \tag{2.1}$$

The gyromagnetic ratio is a constant unique to each individual nucleus, with $\frac{\gamma}{2\pi} = 42.58$ MHz T^{-1} for ^{1}H and -11.78 MHz T^{-1} for ^{129}Xe.

^{1}H and ^{129}Xe are both spin ½ nuclei and can be in one of two possible spin states, $m = \pm 1/2$. Under normal conditions, these two spin states are degenerate, meaning they have the same energy with approximately equal populations in each state. However, due to the Zeeman Effect, in the presence of an external magnetic field the energy for each spin state is

$$E = \gamma \hbar m B_0, \tag{2.2}$$

where ħ is the reduced Plank's constant ($h/2\pi$), m is the spin, and B_0 is the strength of the external magnetic field. The lower energy state, termed spin-up, occurs when the magnetic moment of the nucleus is parallel with the external magnetic field. The higher energy state, termed spin-down, describes when the magnetic moment and external field are anti-parallel.

In conventional magnetic resonance, the number of atoms in each spin state is determined by Boltzmann Statistics. At thermal equilibrium the ratio between the number of atoms in the spin-up and spin-down states is:

$$\frac{N^+}{N^-} = e^{\frac{-\gamma h B_0}{2 k_B T}}, \tag{2.3}$$

where N^+ is the number of spin-up nuclei, N^- is the number of spin-down nuclei, k_B is Boltzmann's constant and T is the temperature. At absolute zero, all of the nuclei are in the lower energy spin-up state and constructively combine to create a strong bulk magnetization. However, as the temperature increases the number of nuclei in each state equilibrates destroying the bulk magnetization.

The nuclear spin polarization describes the population difference between energy states and is defined as:

$$P = \frac{N^+ - N^-}{N^+ + N^-}. \tag{2.4}$$

Under the assumption that thermal energy greatly exceeds the energy difference between spin sates, the Taylor series expansion of Equation (2.3) can be used to express the polarization as:

$$P \approx \frac{\gamma \hbar B_0}{2k_B T} \tag{2.5}$$

At body-temperature in a 1.5 T MRI scanner the polarization of ^{1}H in a 1.5 T MRI scanner is 4.9×10^{-6} and the polarization of ^{129}Xe is 1.4×10^{-6}.

For ^{1}H, the low nuclear polarization level is overcome by the abundance of the protons present. The human body is approximately 70% water, and each gram of water has approximately 7×10^{23} protons available for polarization. Therefore, the signal is not limited by the polarization, but rather the number of protons present and the bulk magnetization can be described as:

$$M_0 = \rho_0 \frac{\gamma^2 \hbar^2 B_0}{4k_B T}, \tag{2.6}$$

where ρ_0 is the density of nuclei.

While this quick signal approximation is appropriate for the majority of the body, it quickly breaks down when examining the lungs. The lungs have an approximate density of 0.30 g/cm^3, signifying low water content. Additionally, air and tissue have very different magnetic properties, and the many air-tissue interfaces in the lung result in significant susceptibility artifacts and loss of signal.

Instead of using a biologically present source, such as ^{1}H, to examine the lungs, a ^{129}Xe gas can be inhaled and used as the signal. The problem with using a gas as the signal source is the nuclear density is four orders of magnitude smaller than the density of protons in water. Thus, a hyperpolarized (HP) ^{129}Xe gas must be employed that has a polarization far above thermal equilibrium. The bulk magnetic signal for a hyperpolarized gas is:

$$M_0 = \frac{1}{2}\rho_0 \gamma \hbar B_0 P. \tag{2.7}$$

Note that the signal is dependent on the polarization levels achievable. Through hyperpolarization, the nuclear spin polarization of ^{129}Xe can be increased five orders of magnitude above thermal polarization level, providing enough signal to perform ^{129}Xe MR imaging and spectroscopy.

2.1.2 Polarization Technique

Hyperpolarization of ^{129}Xe is achieved using a two-step procedure called spin-exchange optical pumping (SEOP) [14]. The first step, optical pumping, uses a laser to polarize the electrons in the valence shell of rubidium (Rb) atoms. The Rb is heated in a glass cell to create a vapor and is exposed to a 795-nm, circularly polarized laser. Each photon in the laser carries exactly one quantum (+ħ) of angular momentum. The wavelength of the laser corresponds to the energy needed to excite the principal electric dipole (D_1) transition of the valence electron. When a Rb valence electron interacts with a photon from the laser it is excited from a ground state ($5s_{1/2}$) into the first excited state

($5p_{1/2}$) as shown in Figure 2b. Both the ground and excited states can have a total angular momentum of ± ½. To conserve angular momentum, only the spin-down ground state can absorb the laser light carrying +*h* of angular momentum and transition into a spin-up excited state. The excited electrons then quickly relax down to the ground state through collisions repopulating both spin states equally [15, 16]. Since only the spin-down ground spin states can absorb the laser light, almost all of the electrons will end up in the non-absorbing spin-up state. Optical pumping can create electron spin-polarizations approaching 100% [17].

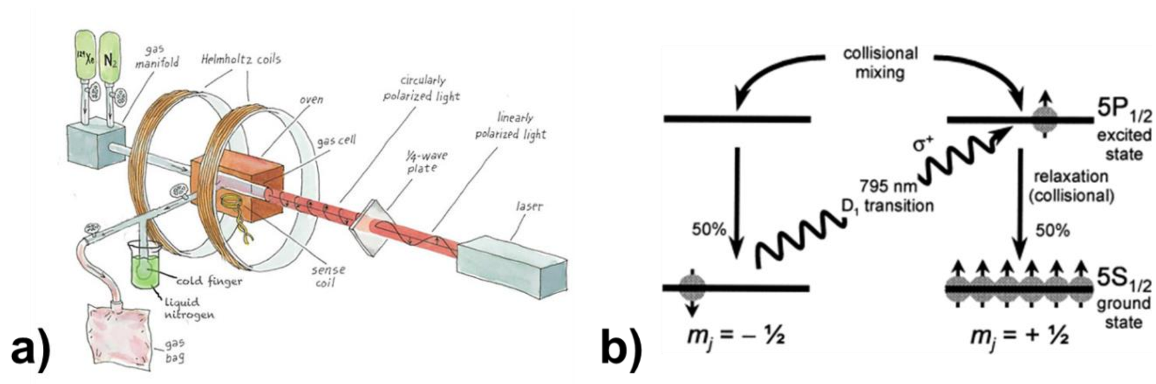

Figure 2. (a) A diagram of the SEOP technique used to polarized ^{129}Xe. *–S. Kadlecek Am Sci 2002;90:540-549 [18]* **(b) Rb optical pumping diagram. The only allowed excitation is represented by the wavy line. The sin-up $5S_{1/2}$ is optically transparent to the laser light.** *–H. Moller MRM 2002;47:1029-1051 [19]*

The second step of SEOP is the spin-exchange from the Rb electrons to the ^{129}Xe nucleus [20]. This exchange occurs when the atoms collide. During the collision, a Fermi contact interaction occurs due to the overlap of the electron and nuclear wavefunction, and there is a transfer of angular momentum. After the collision, the Rb electron is in the spin-down state and is able to absorb additional laser light, and the ^{129}Xe nucleus is in a spin-up state. Maximum polarization for ^{129}Xe is reached in 10's of seconds.

Despite the fast polarization of ^{129}Xe, it is relatively hard to produce large quantities of polarized ^{129}Xe quickly, due to ^{129}Xe-Rb collisions that depolarize the Rb electrons. To avoid having a high concentration of ^{129}Xe atoms, Driehuys et al. [21] developed a method where a gas mixture containing a low percentage of ^{129}Xe flows continuously though a cell (Figure 1a). After the polarized ^{129}Xe exits the cell it is cryogenically separated from the carrier gases by flowing it though a "cold finger" that is submerged in liquid N_2. The hyperpolarized ^{129}Xe remains frozen until the desired volume of gas has been accumulated. The frozen ^{129}Xe is then thawed and dispensed into a dosing bag. This method can produce polarizations approaching 50%.

2.2 Cardiopulmonary Anatomy, Physiology, and Pathology

With ^{129}Xe magnetic resonance, we seek to examine the fundamental function of the lung – gas exchange. The following is a brief overview of the cardiopulmonary anatomy, physiology, and pathology to frame the importance of this research.

2.2.1 Anatomy

The primary function of the lung is gas exchange between air and venous blood in the pulmonary capillaries. The exchange takes place in two directions, oxygen is transported into the blood, and carbon dioxide is removed. The gas transfer takes place at the blood-gas interface and is entirely facilitated by passive diffusion of gasses from a region of high pressure to low pressure. To meet the demands of all of the tissues and organs in the human body, the structure of the airways in the lungs branches in a fractal pattern, becoming increasingly narrower, shorter, and more numerous, to provide an enormous surface area of 50-100 m^2 in a volume of only 4-6 L. The branching begins with the trachea dividing into the left and right main bronchi and continues down 16 generations to the terminal bronchioles. The terminal bronchioles then continue to divide 7 more generations into the respiratory bronchioles, and alveolar ducts until they terminate at alveolar sacs for a total of 23 generations. The upper 16 generations, termed the conduction airways, do not directly participate in gas exchange, but help transport inspired air to the lower generations called the respiratory zone. It is in this lower region that gas is able to diffuse from the airspace into the adjacent pulmonary capillaries via alveoli, small air sacs with very thin membranes (<1 μm). In total, the respiratory zone contains about 500 million alveoli in the human lung, and makes up the majority of the lung volume at rest.

The pulmonary blood vessels have a similar branching pattern to the lung airways. The pulmonary artery, carrying deoxygenated blood from the right ventricle of the heart, repeatedly branches with decreasing diameter to become the pulmonary capillaries. The capillaries have a diameter of about 7-10 μm, barely larger than a red blood cell, and are very densely packed to form an almost continuous sheet in the alveolar walls for efficient gas exchange. On average, each red blood cell spends about

750 ms in the capillary network before the blood vessels recombine to form larger veins that transport the now oxygenated blood into the left atrium of the heart for circulation.

2.2.2 Gas Exchange

Pulmonary gas exchange is dependent on three processes: ventilation, diffusion, and perfusion. Often, diseases can be differentiated by how they affect one or more of these functions. Therefore, it is vital to identify the underlying causes of lung function impairment to aid in accurate diagnosis.

Ventilation describes the movement of air into and out of the pulmonary parenchyma. During inspiration, the diaphragm contracts and moves down while the intercostal muscles pull the ribs upwards and forwards. The lungs passively expand to fill the space and a negative pressure is created that directs the flow of gas into the lungs. Conversely, exhalation occurs due to the positive pressure generated from reduced lung volume as the muscles relax. Diseases such as asthma and chronic obstructive pulmonary disease (COPD), manifest in the upper airways and regionally restrict ventilation [22].

The rate of diffusion is governed by Fick's law and states that gas transfer across a membrane is proportional to its surface area and inversely proportional to its thickness. Consequentially, changes to alveolar shape or membrane thickness can have a huge impact on lung function. For example, when alveolar membranes are damaged or destroyed in emphysema there is reduced surface area available for diffusion of oxygen and carbon dioxide. Alternatively, in idiopathic pulmonary fibrosis (IPF), the thickening of the interstitial tissue decreases the rate of diffusion and subsequently reduces gas exchange.

Finally, perfusion describes the blood flow in the pulmonary capillaries, which can be inhibited or reduced due to pulmonary obstructions, embolisms, or vascular damage. In addition, an inequality between ventilation and perfusion will reduce gas exchange efficiency because of mismatched partial pressures.

2.2.3 IPF

Idiopathic pulmonary fibrosis (IPF) is one of the most common and severe form of interstitial lung disease (ILD), affecting approximately 89,000 people in the United States with 34,000 new patients each year [23]. The disease is chronic, progressive, irreversible, and fatal with a median survival of only 2.5-3.5 years after diagnosis [24]. IPF is characterized by interstitial inflammation and a buildup of excess collagen that reduces diffusion of gas across the alveolar-capillary membrane [25]. By definition, the underlying cause of the fibrosis is unknown.

In about 50% of cases IPF can be diagnosed using high-resolution computed tomography (HRCT) to establish the presence of usual interstitial pneumonia [23, 24]. The remaining cases must be diagnosed through a surgical lung biopsy which carries a non-negligible risk of death and a 20% chance of complications [26, 27]. After diagnosis, pulmonary function tests such as Forced Vital Capacity (FVC) or Diffusing Capacity of the Lung for Carbon Monoxide (DC_{LO}), are the primary methods of monitoring disease progression. However, PFTs are imprecise, noisy, effort dependent, and require large sustained changes to be considered clinically significant [28]. There are no known cures for IPF, but there are new therapies that have been shown to slow progression [29, 30]. Unfortunately, these therapies come at a high cost and significant side effects, creating an urgent need for accurate methods of predicting therapeutic response and monitoring disease progress.

3 ^{129}Xe Dynamic Spectroscopy

Hyperpolarized (HP) ^{129}Xe MRI is a valuable method for imaging lung structure [31-34] and function [35-40]. The successes of ^{129}Xe as a probe for lung function is largely due to the solubility of xenon blood and biological tissues combined with distinct in vivo chemical shifts based on local environment. The sensitivity of the xenon chemical shift stems from a large loosely bound electron cloud that is easily distorted by different chemical and physical environments causing the nucleus to experience different levels of magnetic shielding. This sensitivity is emphasized by a ~200 ppm chemical shift between gas-phase and dissolved-phase xenon resonances (Figure 3).

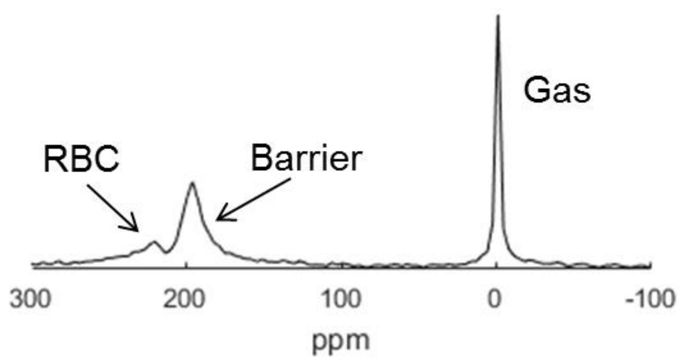

Figure 3. ^{129}Xe Spectrum from the human lung.

The spectral properties of ^{129}Xe have been well characterized in vitro and in vivo. In vitro, ^{129}Xe dissolved in human blood exhibits separate resonances for RBC and plasma separated by approximately 22 ppm [41, 42]. Similarly, in vivo spectra also exhibit two dissolved-phase peaks at 217 and 198 ppm [10]. However, ^{129}Xe dissolved in both plasma and parenchymal tissues have a resonance frequency at 198 ppm, and their individual contributions to the peak are inseparable. Therefore, this resonance is termed the tissue/blood plasma (TP) or barrier peak.

^{129}Xe spectroscopy is rich with information about lung function, gas exchange, and the cardiopulmonary environment. For example, a study by Kaushik et al., found that the relative amplitudes of the dissolved-phase peaks correlates with the diffusing capacity for carbon monoxide (DL_{CO}), a clinically used metric of gas exchange [10]. This study also proposed that ^{129}Xe spectroscopy could be used to detect diffusion impairments in subjects with idiopathic fibrosis (IPF), and discovered six spectral parameters that differed between healthy and IPF populations. Additionally, Wolber et al., found a non-linear dependence of the chemical shift on blood oxygen saturation in vitro (sO_2). This work was confirmed by Norquay et al., and used to approximate the change in sO_2 of a heathy volunteer over a 35s breath hold.

Recently, the temporal dynamics of ^{129}Xe have begun to be explored in a limited number of subjects. Some of this early work reported intriguing preliminary observations [41, 43]. However, only one or two of the four spectral parameters were used to characterize each resonance and the findings were restricted by low temporal resolution. Here, we expand upon this work using higher temporal resolution, and time-domain curve fitting tools to evaluate fast temporal changes in amplitude, chemical shift, line width, and phase for three resonances during a simple breathing maneuver conducted by a cohort of healthy volunteers and subjects with IPF. Furthermore, we seek to test if the temporal dynamics of ^{129}Xe spectroscopy are sensitive to disease.

3.1 Methods

3.1.1 Subject Recruitment

This study was approved by the Duke Institutional Review Board, and written informed consent was provided by all subjects before participation. Dynamic hyperpolarized ^{129}Xe spectra were acquired in 14 heathy subjects and 10 subjects with IPF. Healthy volunteers had no known pulmonary disorders, no cardiac arrhythmias, less than a five-pack year smoking history, and had not smoking in the last 5 years.

3.1.2 ^{129}Xe Polarization and Delivery

Using a commercially available polarizer (Model 9810; Polarean, Inc., Durham, NC), 300 mL of isotopically enriched ^{129}Xe (85%) was polarized to approximately 20%. The polarization occurred via SEOP using a flow-through technique with a gas mixture of 1% Xe, 10% N_2, and 89% He and a 100W 795 nm laser. The Rb was heated to 150 °C to form a vapor before being flowed with the xenon gas mixture at a rate of 1.67 standard liters per minute (SLM) through a glass optical pumping cell. The cell was heated to 120°C to achieve about 60% laser light absorption. As the gas mixture left the cell, the ^{129}Xe was polarized to approximately 30%. The gas then passed through a cold finger submerged in liquid nitrogen (77K) to cryogenically trap the ^{129}Xe (freezing point 165 K) and separated it from the N_2 (freezing point 63 K) and He (freezing point 4 K). The frozen ^{129}Xe was kept in a 200 G magnetic field to extend the T1 to over 2 hrs by reducing thermal depolarization [44]. When 300 mL of gas was accumulated, the liquid nitrogen around the cold finger was replaced with water to thaw the ^{129}Xe. The polarized ^{129}Xe gas was dispensed into a 1-L Tedlar bag (Jensen Inert Products, Coral Springs, FL), and mixed with 700 mL of ultra-high-purity N_2. The bag was kept in a 20 G magnetic field to preserve polarization until it administered to the subject. The polarization was measured using a polarimeter (Model 2881; Polarean, Inc.) immediately after dispensing, and before delivery.

Polarization levels of 20% were routinely achieved corresponding to a dose equivalent of 51 mL. The dose equivalent can be thought of as the equivalent volume of 100% polarized and 100% enriched ^{129}Xe, and is calculated as:

$$DE = f_{129} \times P_{129} \times V_{Xe} \tag{3.1}$$

where f_{129} is the isotropic fraction of ^{129}Xe, P_{129} is the nuclear spin polarization of $^{1`29}$Xe, and V_{Xe} is the volume of xenon gas [45].

Prior to scanning, subjects were instructed to inhale to total lung capacity (TLC), and exhale to functional residual capacity (FRC) twice. The subject was instructed to inhale the gas from the bag through a 6-mm ID Tygon tube, hold their breath for 8 seconds, and then slowly exhale to FRC. Data acquisition began before the subject reached the breath hold. The heart rate and oxygen saturation of each subject was monitored using an MR-compatible monitoring system (Expression Model 865214; Invivo Corporation, Orlando, FL).

3.1.3 ^{129}Xe Dynamic Spectroscopy Acquisition

Dissolved-phase spectra were acquired using a 1.5T GE 15M4 EXCITE MRI scanner (GE Healthcare, Waukesha, WI). Subjects were fitted with a quadrature vest coil tuned to 17.660445 MHz, the gas-phase resonance frequency of ^{129}Xe (Clinical MR Solutions, Brookfield, WI). The dissolved-phase ^{129}Xe was selectively excited using a 1.2 ms 2-lobe sinc pulse at a frequency 3,832 Hz (217 ppm) above the gas-phase. During the 16 second breathing maneuver, 802 ^{129}Xe free induction decays (FIDs) were measured with 512 samples per FID, echo time (TE) = 0.932 ms, repetition time (TR) = 20 ms, receiver bandwidth = 15.63 kHz, flip angle ≈ 20°, spectral resolution = 3.46 ppm. At the end of the dissolved-phase acquisition, a single-shot gas spectrum was acquired using a 17° RF pulse at the gas-phase excitation frequency for use as a reference.

3.1.4 Spectral Improvement by Fourier Thresholding

The signal-to-noise ratio (SNR) of a single-shot ^{129}Xe dissolved-phase spectrum from a dynamic spectroscopy scan is too low to determine the amplitude, chemical shift, line width, and phase for each peak. There are many factors limiting the maximum signal from ^{129}Xe spectroscopy. From Equation (2.7), the NMR signal level from the hyperpolarized gas is

$$S = \frac{1}{2} N \gamma^2 \hbar B_0 P sin(\alpha) \tag{3.2}$$

where N is the number of nuclei excited, γ is the gyromagnetic ratio, ħ is the reduced Plank's constant, B_0 is the field strength, P is the polarization, and α is the flip angle. Since the ^{129}Xe gas is freely diffusing from the airspaces into the barrier tissue and blood stream, the dissolved-phase signal will be replenished after excitation enabling the use of a larger flip angle. However, the size of the flip angle is restricted by off-resonance excitation from the side bands of the hard RF pulse to avoid destroying all of the gas-phase polarization. The number of ^{129}Xe atoms available for excitation is limited by the amount of Xe gas inhaled and the Ostwald solubility of Xenon, which is 0.27 in RBCs [9], and 0.17 in biological tissues [46]. Although, the signal is dependent on the strength of the magnetic field, at the Larmor frequency of xenon ($f_0 = \gamma B_0$), the noise in the sample is dominated by inductive losses which are proportional to the Larmor frequency [47]. Thus, the SNR is essentially independent of field strength. Finally, without further advances in polarization techniques the polarization term will reduce the signal by at least a factor of two.

The analysis of a dynamic spectroscopy acquisition requires both high SNR and high temporal resolution. Often in spectroscopy, SNR is improved by averaging blocks of consecutive spectra together. This approach is appropriate when analyzing a static process; however high temporal resolution is necessary to study the temporal functions of the respiratory and circulatory system. Therefore, the raw FIDs were processed with

Spectral Improvement by Fourier Thresholding (SIFT) before spectroscopic fitting to improve SNR without reducing temporal resolution [48].

The SIFT method is based on the simple assumption that the measured signal is a linear combination of two components: a smooth time-varying signal of interest, and high-frequency white noise. The Fourier transform of the smooth signal will contain a set of coefficients with high amplitudes that correspond to the rate of change in the signal. Conversely, the Fourier transform of the random noise will populate the frequencies with equal likelihood producing a frequency-domain signal devoid of significant coefficients. Since the Fourier transform is a linear operator, the smooth signal can be partially isolated by removing the contributions from frequencies with low intensities. In SIFT this is accomplished by applying a suitable threshold to the Fourier transform of the signal and setting any frequencies with coefficients less than the threshold to zero. For Gaussian noise, a threshold of twice the noise standard deviation decreases the noise value by approximately 86% and removes 95% of frequencies containing only noise [49].

The FIDs underwent de-noising (Figure 1) via the SIFT method in 5 steps. (i) The FIDs were Fourier transformed to obtain the equivalent frequency-domain spectra. (ii) The spectra were then Fourier transformed with respect to the indirect time dimension, or the “TR” domain, to decompose the spectral changes into temporal frequencies. (iii) Any frequency contribution below twice the standard deviation of the noise was set to zero. Noise levels were approximated using portion of the signal corresponding to temporal changes below -20 Hz, and a chemical shift greater than 700 ppm, where no biological ^{129}Xe resonances are known to occur. The chosen threshold suppressed close to 97.5% of frequency coefficients without any noticeable degradation of TR-domain spectral changes. (iv) The thresholded data was inverse Fourier transformed in the TR-domain to return to frequency-domain spectra. (v) The FIDs of the spectra were calculated though an inverse Fourier transform in the direct time domain. The SNR was further improved before spectroscopic fitting by applying a 300 ms (15 FIDs) boxcar filter to the processed FIDs.

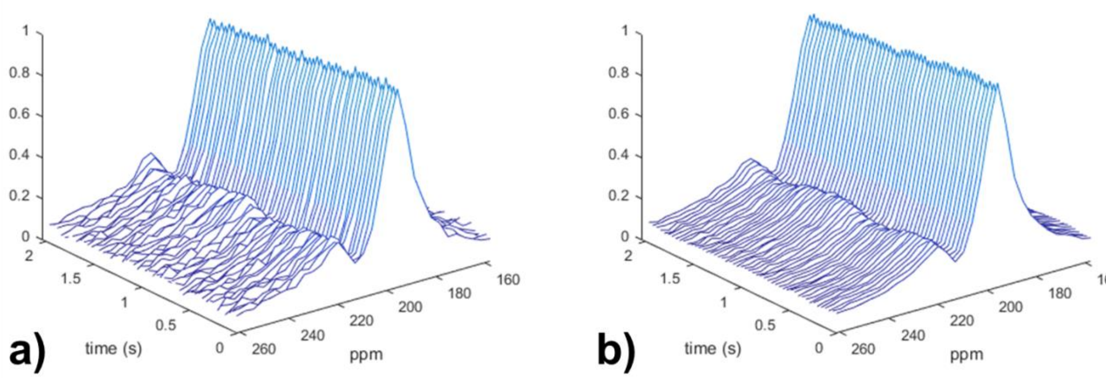

Figure 4. Waterfall plots displaying the magnitude of 50 ^{129}Xe dissolved-phase spectra from a dynamic spectroscopy scan of a healthy volunteer (subject 64). (a) The Fourier transform of the raw FID. (b) The same data after the SIFT method is applied. The temporal changes are smoother and there is a 35% improvement in the SNR of the fit (from 17.8 ± 0.5to 24.1 ± 1.9).

3.1.5 Time-domain Fitting

The free induction decay data were imported into MATLAB (MathWorks, Inc, Natick MA) and processed using a custom toolkit [50]. This open-source code is available for academic use and can be downloaded from www.civm.duhs.duke.edu/NmrSpectroscopy. The toolkit processes the complex FID data by modeling the signal as a linear combination of decaying exponential functions equivalent to Lorentzian peaks in the frequency-domain [51]. Each function is allowed to have a unique amplitude, resonant frequency, line width, and starting phase. The complex signal was curve fit using an iterative trust-region-reflective least squares algorithm [52] to

$$S_{fit}(t, a_k, f_k, w_k, \varphi_k) = \sum_{k=1}^{K} a_k e^{i\varphi_k} e^{2\pi i f_k t} e^{-\pi \Gamma_k t} \tag{3.3}$$

where K is the number of resonance frequencies, t is time, a_k is amplitude, f_k is the central resonant frequency, Γ_k is the full width at half maximum (FWHM) of the corresponding Lorentzian peak, and φ_k is the phase at t = 0. In conventional spectroscopy, the integral of the spectral peak is reported instead of its amplitude. Here, the amplitude of the time-domain signal is reported which, due to properties of the Fourier transform, is equal to the area of the spectral peak.

Complex time-domain fitting has many benefits over more traditional frequency-domain approaches. Many traditional methods require phase corrections to shift the majority of the signal into the real component before discarding the remaining imaginary portion. Thus, any of the data that are not properly phased with simple zeroth and first order corrections are inadvertently discarded and the resulting fit does not necessarily reflect the original spectral structure. In addition, this time-domain technique requires no line broadening, zero padding, or parameter constrains.

All dynamic spectroscopy data was initially fit to three resonances representing two dissolved-phases, RBC and barrier, and one gas-phase. For each resonance the amplitude, chemical shift, line width, and phase were reported and plotted as a function of time.

3.1.6 Converting Frequency to Chemical Shift

To remove the dependence of the reported frequency on daily fluctuations in the magnetic field strength, all frequencies (Hz) were converted to chemical shifts (ppm) using ^{129}Xe in the large airways as the reference frequency. This resonance has been shown to exhibit the most stable frequency [50]. The chemical shift was adjusted by 0.03 ppm for Xe-Xe collisions for a Xe partial pressure of 0.3 atmospheres [53]. The ^{129}Xe large airway frequency was determined by decomposing the dedicated gas spectrum in to two separate resonances for ^{129}Xe in the large airways and alveoli [54]. If the dedicated gas spectrum exhibited over-ranging artifacts then the reference frequency was calculated using the gas-phase contamination signal due to off-resonance excitation in the dissolved-phase acquisition.

The RBC and barrier resonances are found at approximately 217 ppm and 198 ppm respectively [10].

3.1.7 Normalizing, Detrending, and Quantifying Spectroscopic Changes

To correct for signal decay during the breath hold, the amplitude of the signal from resonance was fit to an exponential decay function of the form $A\exp(-t/T1_{\text{app}})$ where $T1_{app}$ is the apparent T_1 (Figure 5). The apparent relaxation rate is not analogous to the true T_1 of xenon in the gas-phase because the signal was not corrected for off-resonance RF excitation. There is a non-uniform dependence of decay rate on lung inflation level [55]; therefore, $T1_{app}$ was calculated separately for each resonance. At TLC the resonances have very similar decays, however at residual volume (RV) a single decay constant cannot be used to correct all three resonances. The breath hold in this study was performed at a lung volume of FRC + 1L, corresponding to approximately 60% of TLC for healthy volunteers and 80% of TLC for subjects with IPF. The pulsation frequency was estimated as the dominant frequency in the autocorrelation of the RBC amplitude after normalization.

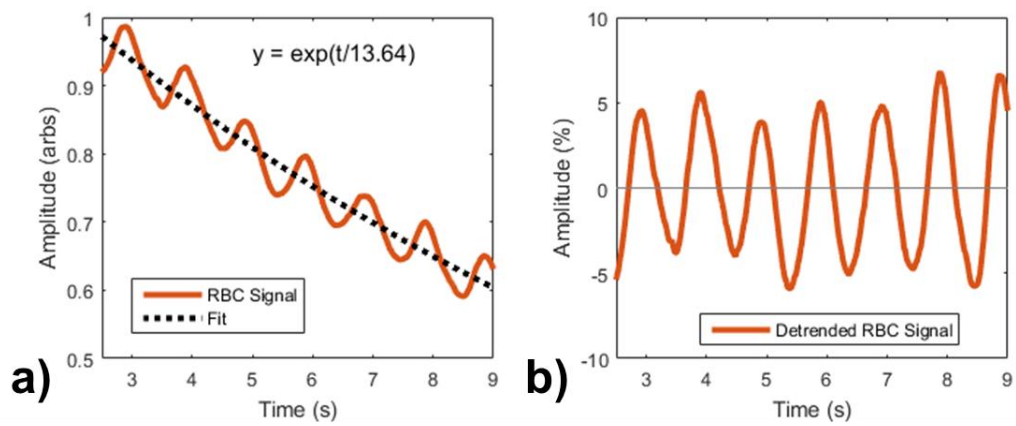

Figure 5. (a) The RBC signal decay over a breath hold. The black dashed line is the exponential fit. (b) The RBC signal normalized to the decay function in (a).

The slow temporal changes in all other peak parameters were simulated by applying a 1 s (50 FIDs) boxcar filter to the FIDs after the SIFT method. The subsequent time-averaged signal was subtracted from the original fit to visually isolate fast spectroscopic changes.

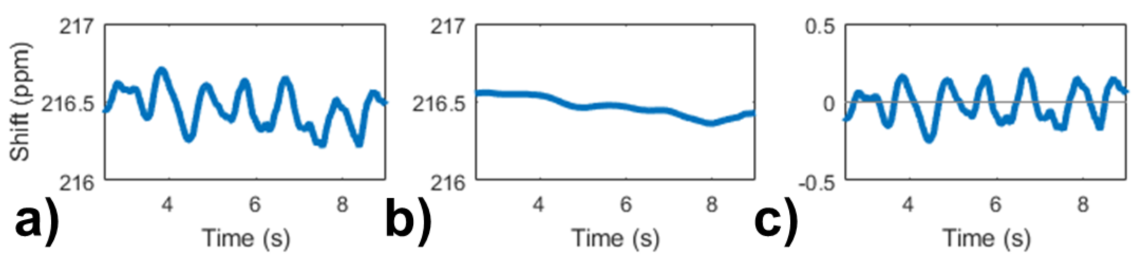

Figure 6. (a) The chemical shift as a function of time. (b) The time-averaged signal used for detrending. (c) The detrended chemical shift.

To quantify the magnitude of the spectral oscillations, the local temporal extrema were identified during the breath hold and the difference between the mean of the maxima and minima was used as an approximation for the peak-to-peak amplitude

(Figure 7). For the spectral amplitude, this calculation was performed after the $T1_{app}$ correction, and was expressed as a percentage of the original signal.

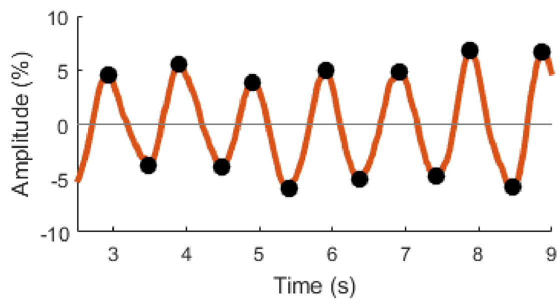

Figure 7. The magnitude of the spectral oscillations was quantified as the peak-to-peak amplitude by identifying local extrema (black dots).

3.1.8 Statistical Analysis

Statistical analysis was performed in MATLAB. A Mann-Whitney-Wilcox U-test was used to determine if differences between healthy normal and IPF subjects were statistically significant (P < 0.05). Outliers were defined as values greater than $q_3 + 1.5(q_1 - q_3)$ or less than $q_1 - 1.5(q_1 - q_3)$ where q_1 and q_3 are the 25th and 75th percentiles of the data.

3.2 Results

3.2.1 Dynamic Spectroscopy of a Representative Healthy Volunteer

Figure 8 displays the change in ^{129}Xe spectroscopic parameters over time for a representative healthy volunteer. The arrows in Figure 8 highlight some of the spectroscopic changes that accompany the breathing maneuver.

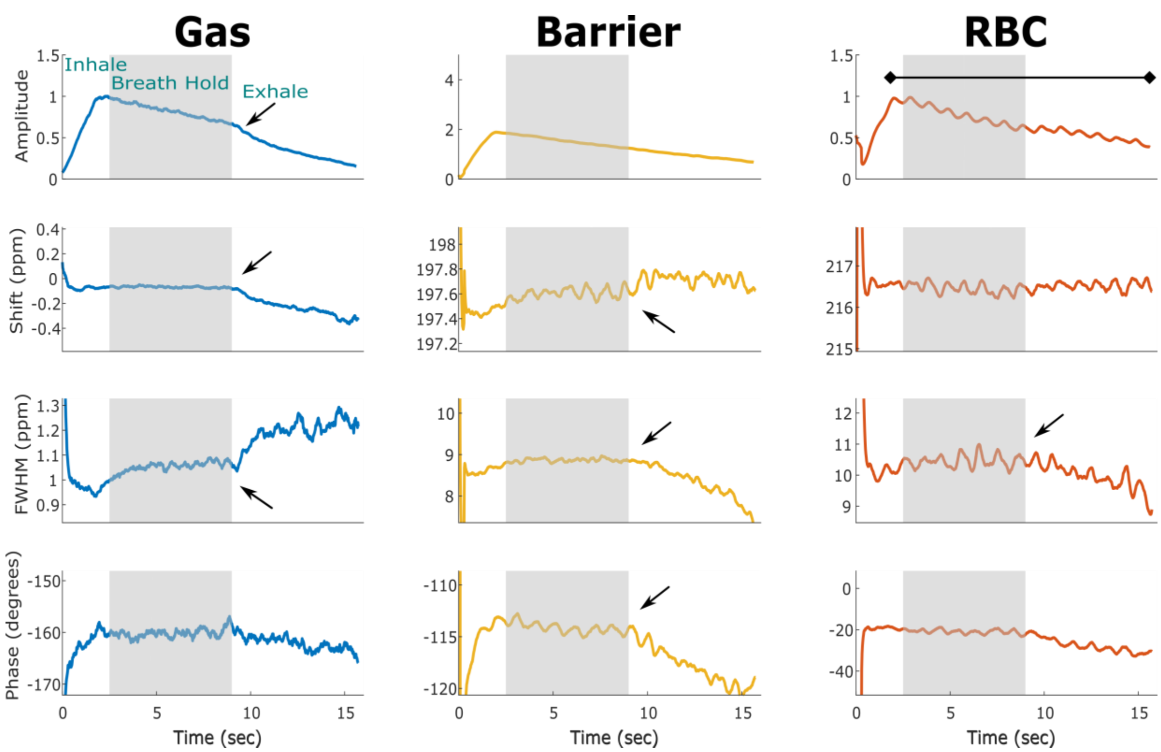

Figure 8. Temporal changes in the spectroscopic parameters of the ^{129}Xe gas, barrier, and RBC resonances in a healthy subject during inhalation, breath hold (gray bar), and exhalation. All intensities are normalized to the maximum gas-phase ^{129}Xe signal.

The breathing maneuver is reflected in each of the gas phase spectral parameters, showing both inhalation and exhalation effects on amplitude, chemical shift, and line width. The gas-phase amplitude decays with an apparent T_1 of 11 s during the breath hold, while the other gas-phase spectral parameters remain fairly constant. As the subject exhales, the gas resonance shifts negatively, by 0.11 ppm, and broadens by 0.2 ppm. The breathing dynamics are also easily seen in the barrier resonances, although exhalation has the opposite effect on the chemical shift and line width. After inhalation, the RBC amplitude exhibits a prominent oscillation. These pulsations also occur, albeit less noticeably, in the RBC chemical shift, line width, and phase. During the breath hold, the mean RBC chemical shift remains largely unchanged.

The spectroscopic parameters of the dissolved-phase resonances during the breath hold period were normalized, and detrended to isolate the oscillatory signal. The zero-mean signal for each spectral parameter in the RBC resonance is displayed in Figure 9a. The oscillation frequency of the amplitude of the signal, 0.98 Hz or 58.60 bpm, is consistent with the pulse rate of the subject measured before and after dynamic spectroscopy, 64 and 63 bpm. The mean peak-to-peak variation in the RBC signal amplitude is 10.3%. The other spectral parameters also oscillate at the cardiac beat frequency, although there is more variation in the value of the local extrema. The chemical shift is the only spectral parameter with oscillations that are in-phase with the RBC signal amplitude modulations. The line width and phase have a phase difference of approximately 180° from the signal amplitude.

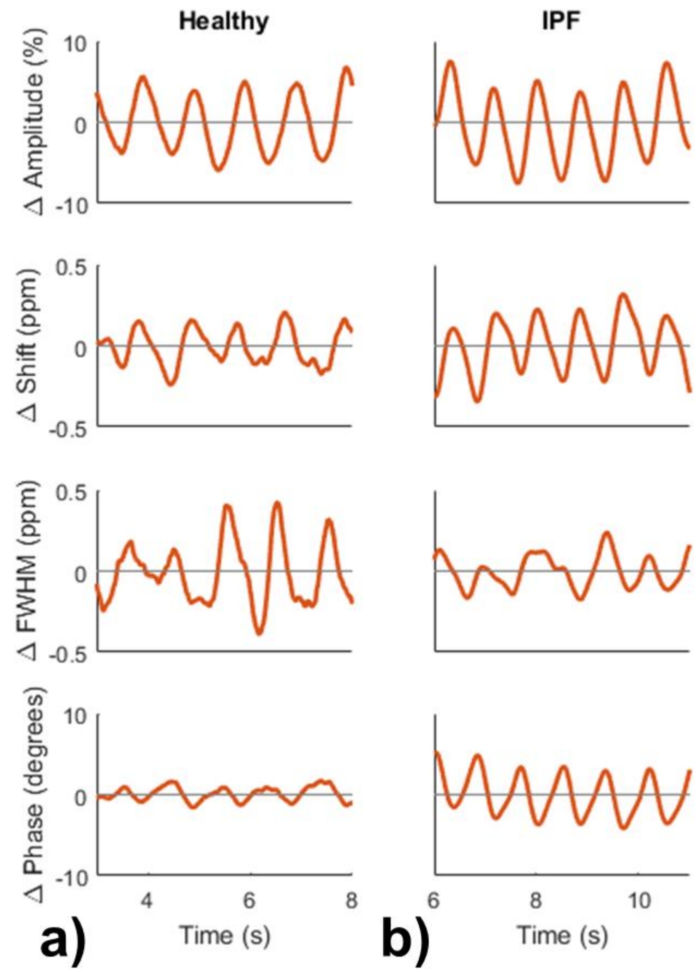

Figure 9. The normalized and detrended RBC spectral parameters for 5 s of the breath hold from a (a) healthy volunteer and (b) subject with IPF.

3.2.2 Dynamic Spectroscopy of a Representative Subject with IPF

Figure 10 displays the same dynamic spectroscopic information for a subject with IPF. Again, the gas-phase parameters reflect the inhale and exhale dynamics, along with a clear increase in the chemical shift and decrease in the line width of the barrier resonance upon exhale. Similar to the healthy subject, the RBC amplitude oscillates at the heart rate, but its chemical shift starts almost 2 ppm lower than the healthy volunteer, and decreases by 0.5 ppm during the breath hold. The most prominent difference from the healthy subjects is the oscillatory behavior is clearly present in the RBC chemical shift and phase.

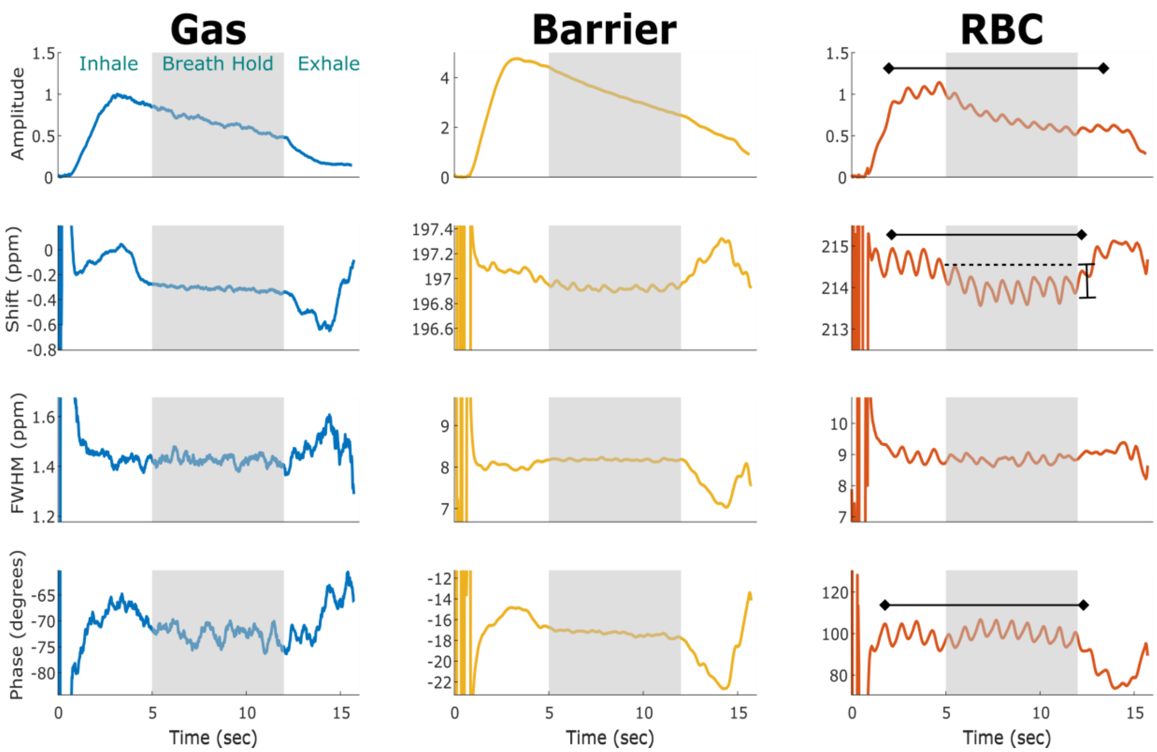

Figure 10. Temporal changes in the spectroscopic parameters of the ^{129}Xe gas, barrier, and RBC resonances in a subject with IPF during inhalation, breath hold (gray bar), and exhalation. All intensities are normalized to the maximum gas-phase ^{129}Xe signal. Unlike the healthy subject, the RBC chemical shift decreases throughout the breath hold and there are very noticeable oscillations at the heart rate frequency not only in the RBC amplitude, but also in the RBC chemical shift and phase.

Figure 9b shows the normalized and detrended RBC spectral parameters during the breath hold. Again, the frequency of the amplitude oscillation, 70.3 bpm, is comparable to the subject's pulse rate pre and post scan (70 and 73 bpm). The peak-to-peak variation in the RBC signal amplitude is 11.0%. Unlike the healthy volunteer, the maxima and minima of the chemical shift oscillations are consistent and have a peak-to-peak difference of 0.50 ppm throughout the breath hold. Again, the line width and phase oscillations are 180° out of phase relative to the signal amplitude oscillations, whereas the chemical shift oscillations are in phase with the amplitude.

3.2.3 Peak-to-Peak Amplitude of Oscillations in the RBC Spectral Parameters

The peak-to-peak changes in each of the RBC spectral parameters are displayed in Figure 11. The oscillations in the amplitude of the signal were consistent at 7.8% ± 2.8% between subjects with IPF and healthy subjects ($P = 0.84$). The line width oscillations are also indistinguishable between the two cohorts ($P = 0.50$). However, subjects with IPF have a 0.45 ppm larger chemical shift oscillations (0.63 ± 0.32 ppm, $P < 0.001$) and 6.5° larger phase oscillations (8.85 ± 3.72 degrees, $P = 0.0012$) than healthy volunteers (0.19 ± 0.06 ppm, 2.39 ± 0.57 degrees).

There is a strong correlation between the peak-to-peak amplitude of the RBC chemical shift and phase ($r^2 = 0.94$), but no correlation between any of the other RBC spectral parameters (Figure 12). The correlation between chemical shift and phase is unsurprising because nuclei with a higher chemical shift by definition have a higher Larmor frequency and will subsequently have more phase accumulation.

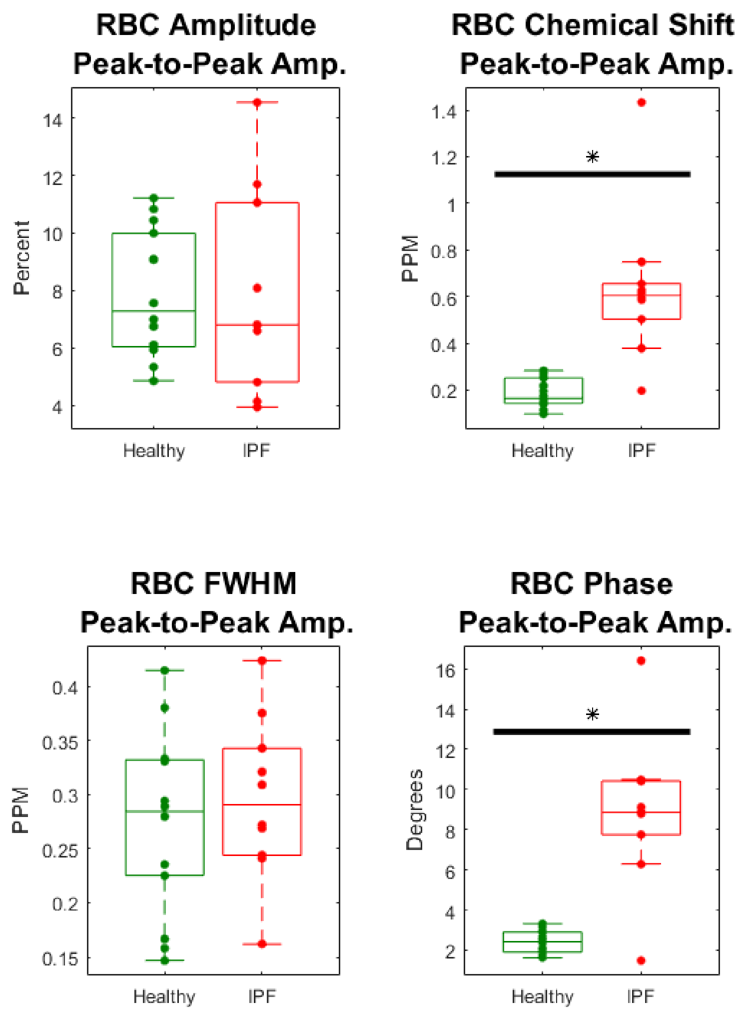

Figure 11. Peak-to-peak variations in RBC spectral parameters over a breath hold for 14 healthy and 10 IPF subjects. Oscillation amplitudes in the RBC chemical shift and phase are significantly larger for IPF subjects than healthy volunteers ($p < .001$ and $p = 0.0012$).

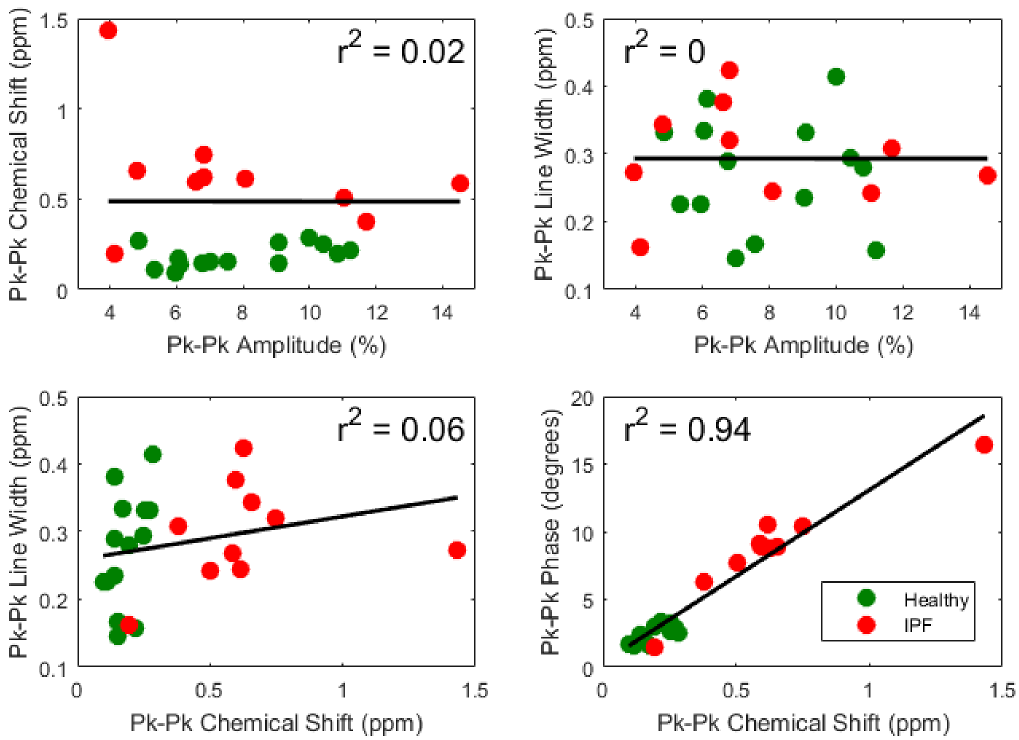

Figure 12. There is a strong correlation between the peak-to-peak amplitude of the chemical shift and phase. No correlations were found between any other parameters. Green circles represent healthy volunteers, red circles represent subjects with IPF, and the black line represents the linear fit.

3.3 Discussion

3.3.1 Origins of Temporal Dynamics

The temporal changes in the ^{129}Xe spectra are a direct reflection of physiological changes in the lung and pulmonary capillaries. It is striking to find that nearly all of the spectral parameters reflect dynamics associated with the breathing maneuver. The exhale is especially well defined by an increase in the gas-phase line width and a corresponding narrowing of both dissolved-phase peaks. Since the line width of a

Lorentzian is inversely related to the apparent transverse relaxation time, T_2^*, the change in line width suggests a change in local field inhomogeneities. Air and tissue have a bulk susceptibility difference of $\Delta\chi \approx 9$ ppm [56] that cause major susceptibility artifacts and line broadening. Upon exhale, air is forced out of the alveolar sacs and there is a reduction in aggregate alveolar volume and alveolar pressure [57-59]. The decrease in mean alveolar inflation corresponds to an increased surface area to volume ratio and increases the number of xenon atoms at the air/tissue interface. This redistribution of gas-phase xenon atoms into areas with more field inhomogeneities has the potential to increase the line width. Also upon exhale, there is an increase in the mean capillary diameter and an increase in average alveolar wall thickness [60-62] . This would reduce the number of dissolved-phase xenon atoms at air-tissue boundaries and potentially explain the decrease in the RBC and barrier line widths.

The RBC signal is assumed to arise predominantly from RBCs in the pulmonary capillary beds. The spatial localization stems from using a low TR (50 ms) in relation to the RBC transit time (~750 ms). Thus, as the blood leaves the gas exchange region all of the ^{129}Xe signal will be destroyed by RF pulses and have no means of replenishment. Any polarization that remains after leaving the pulmonary veins will decay as the blood travels through the systemic circulatory system. Therefore, the fluctuations in the RBC resonance provide evidence that gas exchange is temporally dependent on the cardiac cycle.

The oscillations in the amplitude of the RBC signal are caused by a cyclic change in the number of polarized ^{129}Xe atoms interacting with RBCs. This can occur from cyclic change in the volume of RBCs, or from another physical mechanism modulating the number of ^{129}Xe atoms that are able to transfer from the gas-phase into the capillaries. The former is more likely, as studies have shown that the pulmonary capillary blood volume is dependent on the cardiac cycle [63]. However, it is unknown if this increase is a function of increased flow velocity, increased capillary diameter, or the opening of additional capillaries through recruitment.

In contrast with the peak-to-peak amplitude change in the RBCs of 7.9 ± 0.03%, the maximum changes in the barrier signal were only 2.1% ± 1.4%. Currently, there are conflicting reports on the presence and magnitude of oscillations in the barrier-phase amplitude. Ruppert et al., who first observed the barrier signal pulsations, measured average pulsation amplitudes in the barrier resonance to be about 10 times lower than the RBC oscillations [43], whereas Norquay et al, observed the barrier pulsations to be about half the height of the RBC pulsations [41]. Norquay also presented a potential method of calculation hematocrit (HCT), the volume percent of red blood cells in whole blood, by assuming that the oscillations in the barrier signal are due to changes in the plasma volume. However, the Fahraeus effect states that HCT is dependent on vessel diameter [64, 65] and since mean vessel diameter varies with lung inflation level it presents the possibility that the varying reports of barrier signal oscillations are due to different lung inflation levels.

The relationship between the RBC chemical shift oscillations and cardiac pulsations is more complex. A non-linear relationship between the RBC chemical shift and blood oxygenation level, sO_2, was originally reported by Wolber et al. [42], and recently confirmed by Norquay et al [41]. Completely deoxygenated blood is separated from the plasma peak by 20.4 ppm. As sO_2 increases to 1.0, fully oxygenated blood, the chemical shift increases exponentially by over 5 ppm. The majority of the variation in chemical shift, 4 ppm, is exhibited over physiologically relevant blood oxygenation levels, sO2 = 0.6 – 0.98. Consequently, the RBC chemical shift is very sensitive to small changes in sO_2. Therefore, pulsations in the chemical shift can potentially be used to measure changes in the sO_2 of blood in the pulmonary capillaries on the timescale of the cardiac cycle.

3.3.2 Dynamic spectroscopy is sensitive to disease

^{129}Xe dynamic spectroscopy measures the temporal changes in the cardiopulmonary environment caused by lung inflation level, blood volume, and blood oxygenation levels. Pulmonary diseases change the local environment of the lung, resulting in an impairment of gas exchange. Therefore, changes ^{129}Xe have the potential to be linked to the onset and progression of disease.

In idiopathic pulmonary fibrosis (IPF), there is a thickening of the interstitial tissue limiting the diffusion of gasses across the alveolar membrane. There were clear differences observed in the RBC resonance of the ^{129}Xe over a breath hold in a healthy volunteer versus an IPF subject. The subject with IPF started with a lower RBC chemical shift, which continued to decrease throughout the breath hold. This indicates that the capillary blood in the IPF lungs starts more poorly oxygenated and does not have enough reserve capacity to maintain a well-oxygenated environment throughout the breath hold. Furthermore, subjects with IPF exhibited a larger variation in chemical shift, and subsequently mean sO_2 level, that was modulated by the cardiac cycle. The blood in a healthy normal volunteer reaches full oxygenation in about 250 ms, or a third of the total capillary transit time meaning the average sO_2 is skewed toward fully oxygenated blood [66]. In contrast, diffusion occurs more slowly in a subject with IPF and consequently sO_2 levels have a more broad distribution. Therefore, although a healthy volunteer and subject with IPF may have the same distal O_2 saturation level, the IPF lung has a wider range in the mean sO_2 in the pulmonary capillaries as the total blood volume changes.

3.4 Study Limitations

3.4.1 Three-dissolved Phase Resonances

Although the dynamics seen in the ^{129}Xe spectra are intriguing and there are significant differences between cohorts, we must carefully ensure that we truly understand the underlying spectral structure. To this end, Robertson et al. recently proposed, based on static spectra, that dissolved-phase ^{129}Xe spectra should be fit to three resonances to more accurately decompose the FID and to eliminate distinct spectral oscillations in the residual error of ^{129}Xe [50]. The three resonances are termed RBC, barrier 1, and barrier 2, although it is hypothesized that barrier 1 originates from the alveolar tissue, and barrier 2 originates from plasma and inflammation in the interstitial space. To evaluate the temporal effects with a three dissolved-phase model, much of the dynamic spectroscopy analysis was repeated assuming the presence of RBC, barrier 1, barrier 2, and gas resonances.

Therefore, we tested how the assumption of three dissolved-phase resonance affects spectroscopic dynamics. This is seen in Figure 13, which displays the change in ^{129}Xe spectroscopic parameters assuming three dissolved-phase resonances for the same representative healthy volunteer shown Figure 8. The breathing maneuver is no longer recognizable in the barrier resonances, although, it is still seen in the gas and RBC phases. For all of the resonances, the spectroscopic parameters have a more random pattern over times, especially in the two barrier resonances. This is caused by a small separation in the chemical shift between the two barrier peaks, 5 ppm on average in healthy volunteers [10], combined with a comparatively low spectral resolution of 3.46 ppm. Compared to the two-dissolved phase mode, the range of the chemical shift for the two barrier peaks is 4 and 7 times higher.

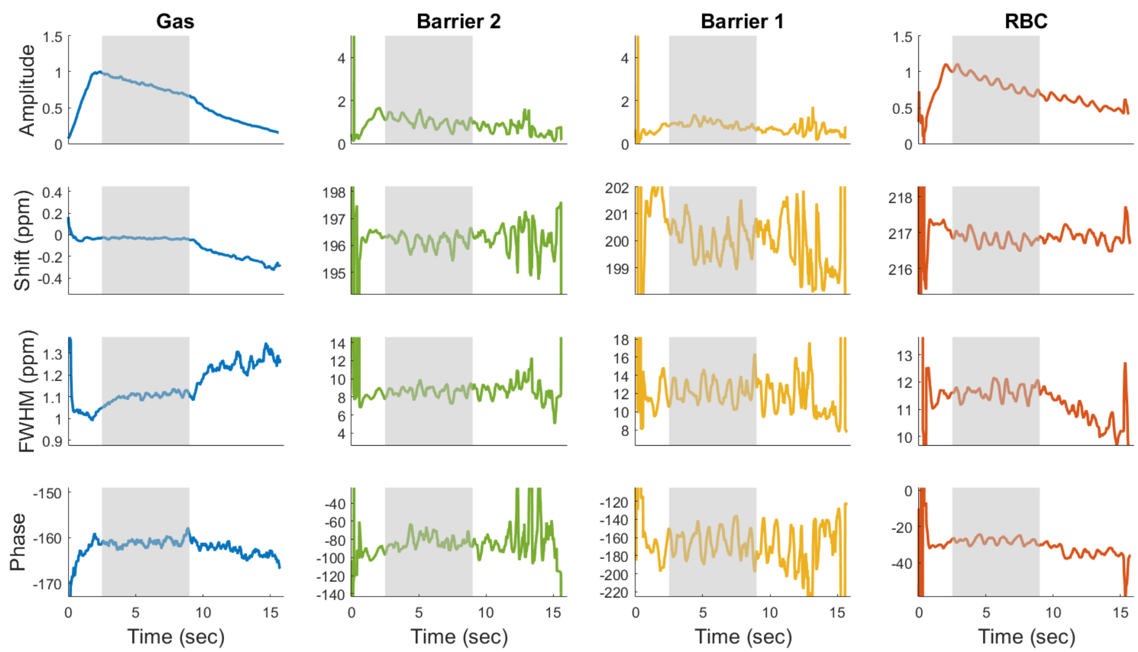

Figure 13. Temporal changes in the spectroscopic parameters of the ^{129}Xe gas, barrier 2, barrier 1, and RBC resonances in a healthy volunteer during inhalation, breath hold (gray bar), and exhalation. All intensities are normalized to the maximum gas-phase ^{129}Xe signal. The chemical shift and line widths have greater variation over the breath hold than in the two dissolved-phase fit.

Figure 14 displays the same information for the subject with IPF in Figure 10. Again, there is a more random pattern to the spectral dynamics. However, the relative stability of chemical shift of the barrier peaks suggests that the spectral separation of the two barrier peaks is more accurate. This is supported by a large difference in the chemical shifts of the barrier peaks along with narrower line widths. In contrast with the two dissolved-phase model, the amplitude of the RBC chemical shift and phase oscillations in the three dissolved-phase model do not appear to differ between subject with IPF and the healthy volunteer.

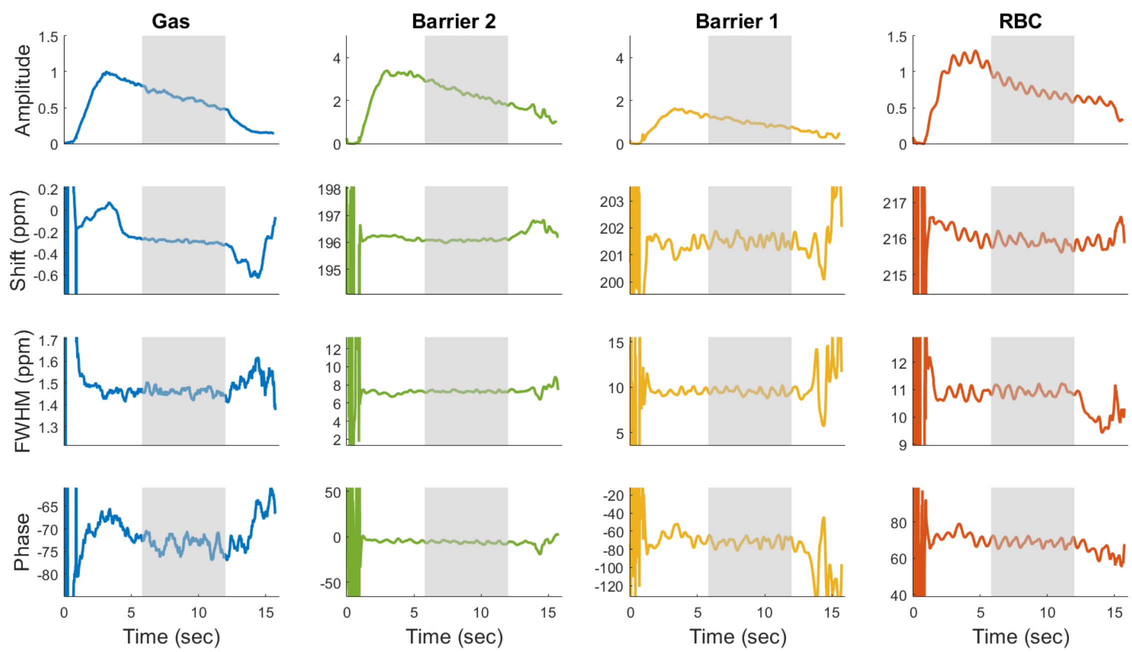

Figure 14. Temporal changes in the spectroscopic parameters of the ^{129}Xe gas, barrier 2, barrier 1, and RBC resonances in a subject with IPF during inhalation, breath hold (gray bar), and exhalation. All intensities are normalized to the maximum gas-phase ^{129}Xe signal. The amplitude of the oscillations in the RBC chemical shift and phase are greatly diminished compared to a two dissolved-phase fit.

The amplitude of the RBC spectral parameter oscillations for the three-dissolved phase fit were calculated and are found in Figure 15. There are no significant differences in the peak-to-peak amplitudes of the RBC signal, frequency, line width, or phase. In healthy volunteers, the addition of a spectral peak increased the peak-to-peak amplitude of the signal and phase oscillations ($P = 0.011$, $P < 0.001$). In subjects with IPF the additional spectral peak did not change the amplitude of the signal oscillations ($P = 0.19$), but it did decrease the size of the frequency, line width, and phase pulsations.

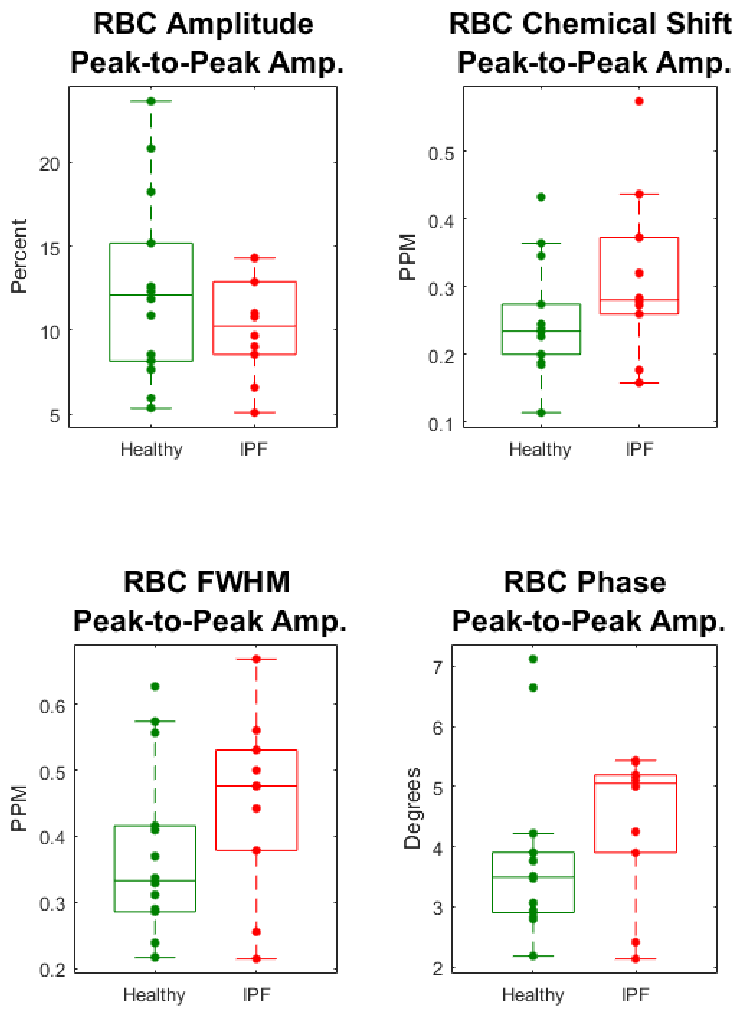

Figure 15. Peak-to-peak variation in RBC spectral parameters over a breath hold using a three dissolved-phase fit. Oscillation amplitudes in the RBC chemical shift and phase are not significantly larger for IPF subjects than healthy volunteers, unlike a fit assuming only one barrier resonance.

Figure 16 displays the relationship between the peak-to-peak amplitude in various spectral parameters. In contrast to the two dissolved-phase fit, there is a correlation between the chemical shift and line width. Additionally, correlation between the chemical shift and phase is weaker in the three dissolved-phase fit.

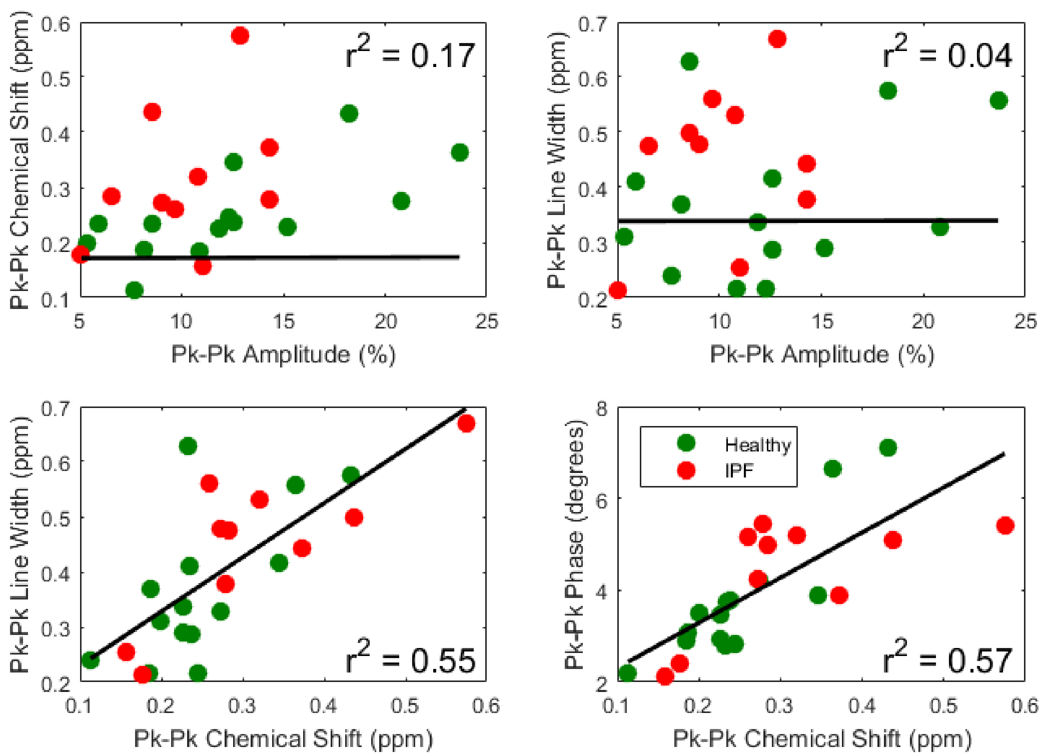

Figure 16. There is a correlation between peak-to-peak amplitude of the chemical shift and line width, and the chemical shift and the phase. Green circles represent healthy volunteers, red circles represent subjects with IPF, and the black line represents the linear fit.

If the temporal dynamics of the ^{129}Xe spectra are best represented using two barrier resonances then the large regular oscillations in the RBC chemical shift in the two-dissolved phase fit are most likely an artifact of the fitting technique. This implies that a certain spectral structure, present only in the three-dissolved phase fit for IPF subjects, causes the changes in chemical shift. Three potential sources of these oscillations are a reduced chemical shift between the RBC and barrier 1 resonance, an increase in the barrier 1 width, and a smaller phase separation between the RBC and barrier 1 peak. No correlation was found between any of these spectral characteristics and the peak-to-peak amplitude of the RBC frequency ($r^2 = 0.18$, $r^2 = .18$, $r^2 = 0.7$). Thus, it is unlikely that the changes in chemical shift with the cardiac cycle in the two-dissolved phase model are attributable to a simple fluctuating misassignment of a portion of the barrier 1 signal to the RBC peak.

It is not clear if the dynamic spectroscopy is best represented by a two or three dissolved-phase fit. Ideally, dynamic spectroscopy would be acquired with higher spectral resolution to aid in the decomposition of the dissolved-phase peaks. However, there is trade-off between spectral and temporal resolution. Alternatively, simultaneous electrocardiography could be used to retrospectively gait the spectra to improve SNR, and match spectral changes to the cardiac cycle.

4 Dynamic Spectroscopy Digital Phantom

Given the challenges of determining the correct spectroscopic model by fitting patient data, it is desirable to test the performance of the fitting code in the context of a ground truth. To this end, we created a digital phantom that simulates the FIDs collected in a dynamic spectroscopy acquisition. The digital phantom was designed to have any number of resonances defined by four spectral parameters (amplitude, chemical shift, line width, and phase). Additionally, temporal oscillations of a specified peak-to-peak amplitude can be individually simulated in any of the spectral parameters at a frequency of 1 Hz. We used this digital phantom to analyze the effects of our spectroscopic analysis on various spectral scenarios.

4.1 Methods

4.1.1 Mathematical Model of Time Varying Signal

The large variation in the amplitude of the components over the breathing maneuver was modeled using exponential functions. The model, shown in Figure 17a, includes a 2 s inhale, 9.4 s breath hold (BH), and a 4.6 s exhale. The exponential growth equation for the inhale was chosen to mimic dynamic spectroscopy data from real subjects.

$$f(t_{inhale}) = \frac{e^{4t}}{3000} \tag{4.1}$$

A normalizing factor of 1/3000 was included to obtain a signal amplitude of 1 at $t = 2$. The model for exhalation was also determined by approximating the decay rate of the gas amplitude from patient dynamic spectroscopy data and is described by

$$f(t_{exhale}) = f(BH_{end})e^{-(t+11.4)/2} \tag{4.2}$$

where $f(BH_{end})$ is the amplitude of the model at the end of the breath hold.

Throughout the breath hold there is free diffusion of ^{129}Xe in the free air spaces into the barrier tissue and blood stream. Typically, it takes 30-40 ms for replenishment of the dissolved-phase ^{129}Xe. This model assumes no off resonance excitation and no dependence on the number of excitations or flip angle and full signal recovery through diffusion. Therefore, the signal decay over the breath hold can be simply described by T1 relaxation with a relaxation time of ~20 s for ^{129}Xe in the human lung [37].

$$f(t_{breath\ hold}) = e^{-\frac{(t+2)}{20s}}. \tag{4.3}$$

Amplitude oscillations were simulated over the breath hold period using a sine function with a frequency of 1 Hz. Oscillations in all other spectral parameters were simulated over the entire acquisition using phase-shifted sine function with the same frequency. The amplitude and chemical shift oscillations were in phase while the phase oscillations were 180° out of phase.

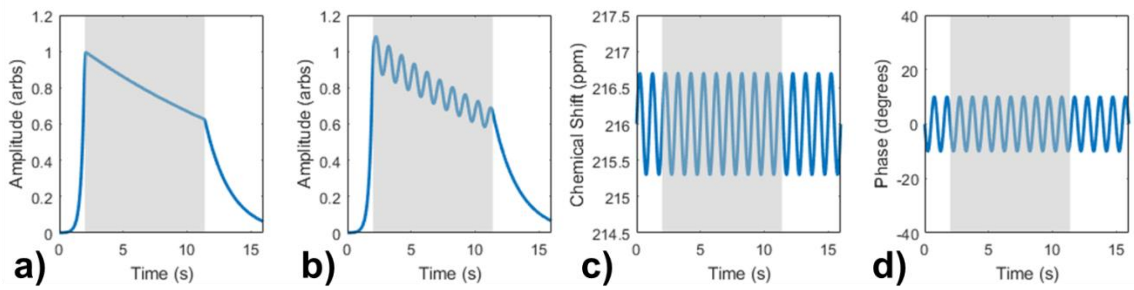

Figure 17. The simulated spectral dynamics and temporal oscillations for (a) the amplitude of the signal, and oscillations in the (b) amplitude (c) chemical shift, and (d) phase. The model mimics the spectral dynamics derived from example subjects with IPF.

4.1.2 Simulating the Time Domain Signal

Each FID in the dynamic spectroscopy phantom was mathematically simulated in the time-domain with 1024 points per FID, a dwell time of 32μs, a TR of 20ms, and a center frequency of 17.660445 MHz. The signal was calculated using the equations for Lorentzian peaks found in Section 3.1.5. The phantom had either 3 or 4 spectral components (2 or 3 dissolved-phases and a gas phase) with each component having an individually defined amplitude, chemical shift, line width, and phase. Oscillations of specified peak-to-peak (pk-pk) amplitudes were simulated on various spectral parameters and peaks. The values for each were chosen based on an IPF model and can be found in Table 1.

Table 1. Values used in digital phantom creation for a 3 and 4 resonance system.

Resonance	Amplitude (arbs)	Chemical Shift (ppm)	FWHM (ppm)	Phase (degrees)
3 Resonances				
RBC (Center Values)	1	216	8	40
RBC Oscillation Amplitude (pk-pk)	10%	0.7	0.3	10
Barrier	4	197	6	50
Gas	1	0	1.5	-70
4 Resonances				
RBC (Center Values)	1	217	11.5	0
RBC Oscillation Amplitude (pk-pk)	10%	0.7	0.3	10
Barrier 1	2	201	11	75
Barrier 2	3	196	7	0
Gas	1	0	1.5	-40

White Gaussian noise was added to the FIDs with 1/3 of the magnitude of the RBC signal to achieve an SNR similar clinical dynamic spectroscopy data. Figure 18 displays a visual comparison of clinical and simulated dynamic spectroscopy data.

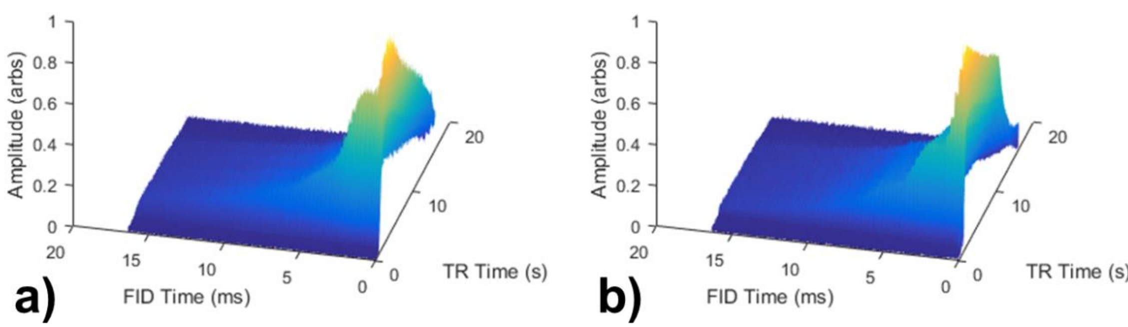

Figure 18. The FID of dynamic spectroscopy from (a) a clinical scan, and (b) the dynamic spectroscopy phantom. FID time represents the dwell time within a single FID, and TR time represents the time at which individual spectra were acquired.

4.2 Results and Discussion

4.2.1 Validation

As a validation for the spectroscopic analysis used in dynamic spectroscopy a phantom was created based on an IPF model and cardiac oscillations were placed in all of the RBC spectral parameters. Figure 19 displays the spectral parameters determined through spectral analysis as a function of time (solid color lines) along with the ground truth of the model (black dashed lines). Generally, there appears to be good agreement of the calculated and modeled parameters. The greatest deviations are at the beginning of the inhale and the end of the exhale where SNR is the lowest. The relative phases of the RBC cardiac pulsations in the chemical shift, line width, and phases are accurately reproduced through fitting.

The spectral dynamics of the fitted parameters were calculated and compared to their known values (Table 2). All of the peak-to-peak amplitudes were underestimated signifying a systematic process. This is most likely due to the 300 ms boxcar filter applied to the FIDs before fitting. The RBC line width had the greatest difference between measured and true peak-to-peak amplitude. Although some of this error can be attributed to the boxcar filter, it is likely that a portion of the difference comes from slightly inaccurate fit. It is encouraging that this effect appears to manifest in the line width instead of the chemical shift, which is theoretically sensitive to blood oxygenation level.

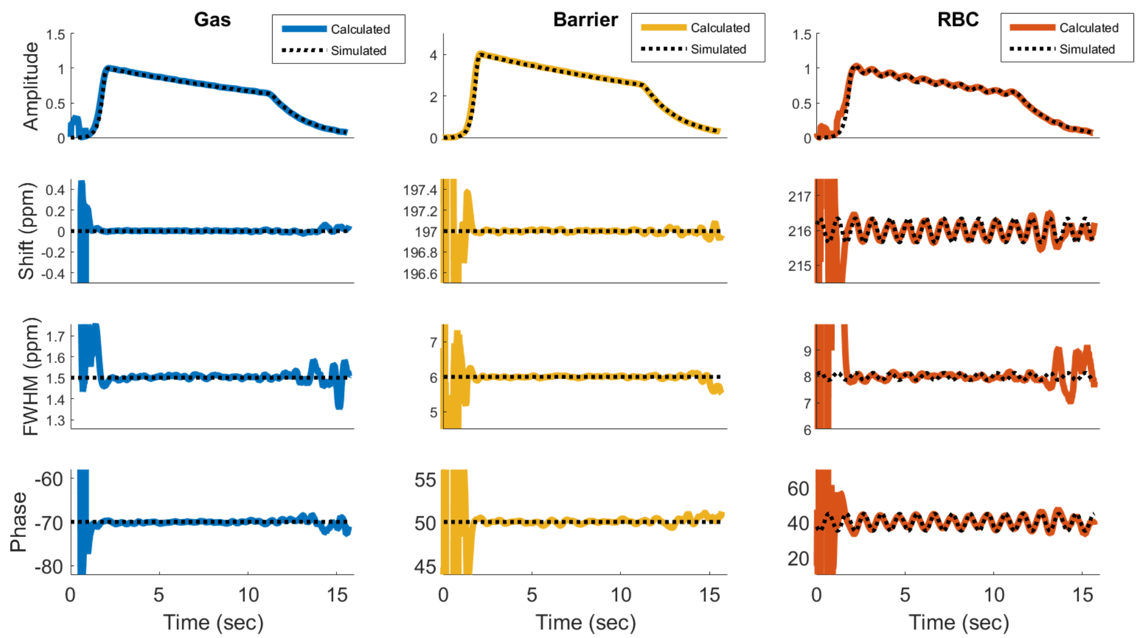

Figure 19. The results of spectral processing, including SIFT and time-domain fitting, on a simulated dynamic spectroscopy data set (solid colored line) with oscillations in all RBC spectral parameters. The ground truth is plotted on the same graph for comparison (black dashed line).

Table 2. The calculated oscillation frequency and peak-to-peak amplitude for each of the RBC spectral parameters. The true oscillation frequency is 1 Hz for all parameters.

RBC Spectral Parameter	Oscillation Frequency (Hz)	Measured Peak-to-Peak Amplitude	True Peak-to-Peak Amplitude	Percent Error
Amplitude	1.03	6.03%	10%	13.8%
Chemical Shift	0.98	0.58	0.7	13.8%
Line Width	1.03	0.18	0.3	39%
Phase	0.98	8.04	10	20%

4.2.2 Simulating a hematocrit of 0.5

The relationship between the oscillation amplitude of the RBC and barrier resonance can be used to estimate hematocrit (HCT) assuming that fluctuations in plasma volume are the source of the barrier signal changes [41]. The relative number of ^{129}Xe atoms, X, interacting with RBCs or plasma is $X = \Delta S/\delta$, where ΔS is the peak-to-peak amplitude of the signal and δ is the solubility of xenon (δ_{RBC} = 0.27, δ_{plasma} = 0.094) [9]. HCT is defined as the volume percent of RBCs in whole blood, or

$$\mathrm{HCT} = \frac{X_{RBC}}{X_{RBC} + X_{plasma}}. \tag{4.4}$$

To calculate a hematocrit of 0.5, approximately the HCT for pulmonary capillaries [67], the barrier signal oscillations must have 1/3 the height of the RBC oscillations. Data was simulated with oscillations only in the RBC and barrier peaks using a peak-to-peak height of 3.5% for the barrier resonance and processed using the standard dynamic spectroscopy methods. The results are shown in Figure 20.

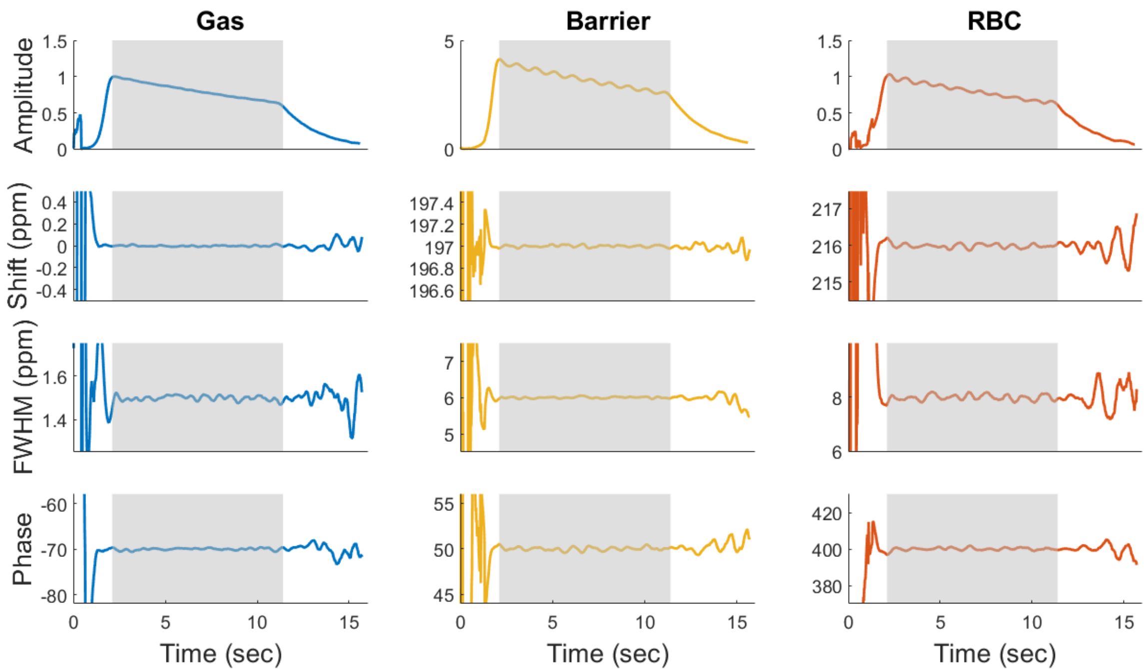

Figure 20. The results of spectral processing, including SIFT and time-domain fitting, on a simulated dynamic spectroscopy data set with oscillations simulated in the RBC and barrier amplitudes.

The calculated HCT from simulated dynamic spectroscopy calculations is 0.43, which closely matches the expected value of 0.5. The 14% difference between the measured and expected value could be caused by spectral averaging from the boxcar filter, the added noise, or incorrect decomposition of the signal into three separate spectroscopic peaks. Another important feature in Figure 20 is the lack of significant oscillations in the RBC chemical shift, line width, and phase, indicating that the oscillations in the spectral parameters are not an artifact of oscillations in signal amplitudes in a two-dissolved phase model.

4.2.3 Fitting to two-dissolved phase peaks when three-dissolved phase resonance are present

The impact of fitting to the incorrect number of peaks was investigated by creating a phantom with 3 dissolved-phase peaks and oscillations only in the RBC amplitude, and then fitting the FIDs to a 2-dissolved phase model. The temporal spectral dynamics for the three fitted peaks are displayed in Figure 22. Fitting to an incorrect number of peaks creates irregular pulsations at the cardiac frequency in all of the RBC spectral parameters. However, the induced oscillations have different characteristics than those observed clinically for a subject with IPF. Foremost, the amplitude of the line width oscillations in the model (0.62 ppm) is almost double the amplitude of the chemical shift oscillations (0.38 ppm), whereas this relationship is reversed in clinical data. Additionally, in the model, the line width oscillations are in phase with the chemical shift oscillations, but in clinical data, the line width and chemical shift are 180° out of phase. There is also a large difference between the magnitudes of the phase oscillations in the digital phantom versus clinical data.

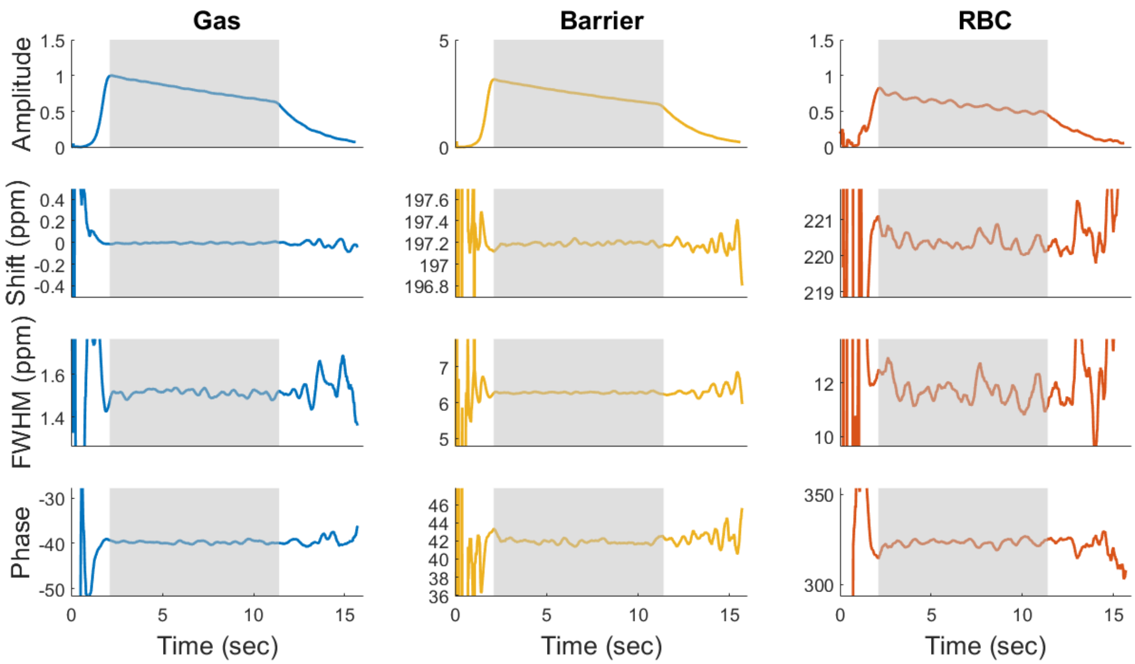

Figure 21. The results of spectral analysis assuming 2 dissolved-phase resonances using a model created with three dissolved-phase peaks. Oscillations were only simulated in the RBC amplitude, yet pulsations appear in all of the RBC parameters.

4.3 Conclusions

The digital phantom is a valuable platform for validating spectral processing and fitting to ensure that the spectral dynamics are an accurate depiction of data in the measured FIDs. It also provides a method for testing theories on spectral structure for comparison with clinical data.

In the future, we would like to use the phantom to investigate the effect of noise on the fitting algorithm and quantify SNR requirements for good reproducibility.

5 Lineshape Analysis

The accurate quantification of the spectral characteristics of dissolved-phase ^{129}Xe is imperative for accurate dynamic spectroscopy. This presents a challenge due to low spectra resolution and SNR. The wild inconsistency in spectroscopic temporal changes between the two and three dissolved-phase models indicates the possibility that neither model accurately represents the physical system. Therefore, higher resolution ^{129}Xe spectra from healthy volunteers and IPF subjects were used to evaluate the possibility of using two peaks with different lineshapes to accurately fit dissolved phase ^{129}Xe in the human lung.

5.1 Methods

To avoid redundancy, only methods specific to the spectroscopic calibration acquisition are described in detail in this section. See Section 3.1 for a more complete account of methods.

5.1.1 Subject Recruitment

This study was approved by the Duke Institutional Review Board, and written informed consent was provided by all subjects before participation. Hyperpolarized ^{129}Xe spectra were acquired in 12 heathy subjects (8 males and 4 females; 32.1 ± 13.8 years old), and 12 subjects with IPF (10 males and 2 females; 68.5 ± 7.2 years old), as a part of a larger imaging protocol. Prior to spectroscopy, all subjects underwent baseline pulmonary function testing to measure FRC, TLC, forced vital capacity (FVC), and carbon monoxide diffusing capacity (DL_{CO}).

5.1.2 ^{129}Xe Polarization and Delivery

Each hyperpolarized ^{129}Xe dose was produced using the methods described in Section 3.1.2.

Prior to scanning, subjects were instructed to twice inhale to TLC, and exhale to FVC twice. The subject was instructed to inhale the gas from the bag through a 6-mm ID Tygon tube and hold their breath for the duration of the 13-second scan. The heart rate and oxygen saturation of each subject was monitored using an MR-compatible monitoring system (Expression Model 865214; Invivo Corporation, Orlando, FL).

5.1.3 ^{129}Xe Calibration Spectroscopy Acquisition

The spectra collected from this scan were also used as a calibration for later imaging sequence, which is why it is referred to as the calibration acquisition. Gas and dissolved-phase spectra were acquired on a 1.5T GE 15M4 EXCITE MRI scanner (GE Healthcare, Waukesha, WI) using a quadrature ^{129}Xe vest coil (Clinical MR Solutions, Brookfield, WI). Over the 13-second breath hold dissolved-phase ^{129}Xe FIDs were measured using the following parameters: 512 samples/FID, TE/TR = 0.875/50 ms, BW = 8.06 kHz, 1.2 ms 3-lobe sinc pulse, flip angle ≈ 22°, spectral resolution = 1.78 ppm. In the same breath-hold, a single gas-phase FID was also acquired using similar acquisition parameters, but with a flip angle of 0.5°. The first 48 dissolved-phase FIDs were discarded to remove any contribution from magnetization that had accumulated downstream of the pulmonary capillary beds. The remaining 38 steady-state dissolved-phase FIDs were averaged together to improve SNR before curve fitting.

5.1.4 Time-domain Fitting

The toolkit and methods described in Section 3.1.5 were used to fit FIDs to different lineshapes.

The two dissolved-phase resonances were individually fit to a model signal representing either a Lorentzian or a Gaussian, the two most commonly used lineshapes in NMR spectroscopy. From Section 2.1.1, the time-domain signal model for a single Lorentzian peak is

$$s_L = a_n e^{i\varphi_n} e^{2\pi i f_n t} e^{-\pi \Gamma_n t} \quad (5.1)$$

where t is time, a_n is amplitude, f_n is resonant frequency, Γ_n is the FWHM, and φ_n is the initial phase. The Gaussian model is

$$s_G = a_n e^{i\varphi_n} e^{2pif_n t} e^{-g_n t^2} \quad (5.2)$$

where $g_n$is the Gaussian decay constant and is related to the FWHM by $g_n = 8\ln(2)\,\Gamma_n^2$.

An additional signal used for the barrier tissue resonance is as a linear combination of two Lorentzian signals where one is completely dependent on the other as described by

$$s_B = a_n e^{i\varphi_n} e^{2\pi i f_n t} e^{-\pi \Gamma_n t} + A a_n e^{i(\varphi_n + D)} e^{2\pi i (f_n + B) t} e^{-\pi C \Gamma_n t}. \quad (5.3)$$

The parameters A, B, and C, are derived from the barrier 1 and barrier 2 resonances in a three dissolved-phase model and are shown in Table 3 for healthy and IPF populations. This fitting scheme is termed the “barriers” model and abbreviated L+L.

The spectral lineshape for the five two-dissolved phase models is depicted in Figure 22.

The total residual error of the fit is defined as the sum of the absolute difference between the measured FID and the time-domain signal calculated using the fit parameters.

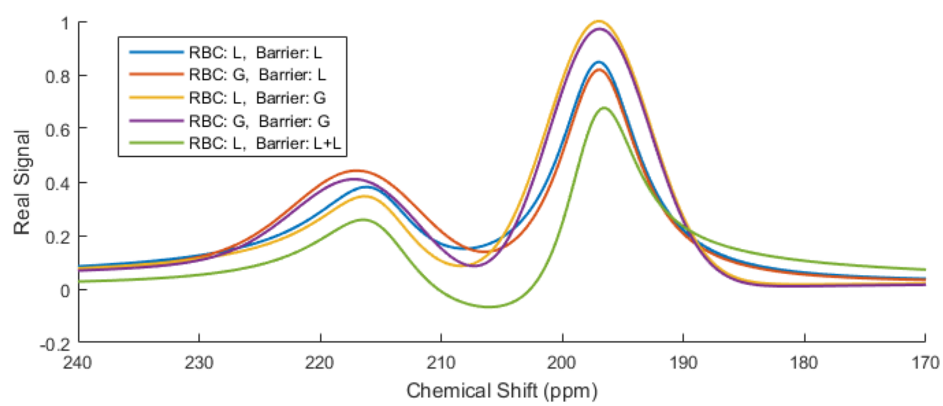

Figure 22. An example spectrum for each fit model. Peaks are at 215 and 197 ppm with a 1:2 area ratio and a 20° phase separation.

Table 3. Parameter definitions and values used to fit the barrier resonance to a linear combination of an independent and dependent Lorentzian.

Parameter	Definition	Healthy	IPF
A	$\frac{\text{amplitude}_{\text{barrier1}}}{\text{amplitude}_{\text{barrier2}}}$	0.71 ± .14	0.81 ± .18
B	$\text{freq}_{\text{barrier1}} - \text{freq}_{\text{barrier2}}$	4.9 ± .7 ppm (87.3 ± 12.3 Hz)	5.3 ± .5 ppm (92.9 ± 9.4 Hz)
C	$\frac{\text{line width}_{\text{barrier1}}}{\text{line width}_{\text{barrier2}}}$	1.6 ± .2	1.6 ± .1
D	$\text{phase}_{\text{barrier1}} - \text{phase}_{\text{barrier2}}$	218.1 ± 16.1°	233.5 ± 8.7°

5.2 Results

5.2.1 Residual Error

The FIDs for 12 healthy volunteers and 12 IPF subjects were fit using two dissolved-phase peaks to five different combinations of signal models: both Lorentzian (LL), RBC Gaussian and barrier Lorentzian (GL), RBC Lorentzian and Barrier Gaussian (GL), both Gaussian(GG), and RBC Lorentzian and barrier fit to the dependent barriers model (barriers). The data from all subjects was also fit to three Lorentzian dissolved-phase peaks (LLL). The results of the six fitting schemes for a representative healthy volunteer and IPF subject is displayed in Figure 23.

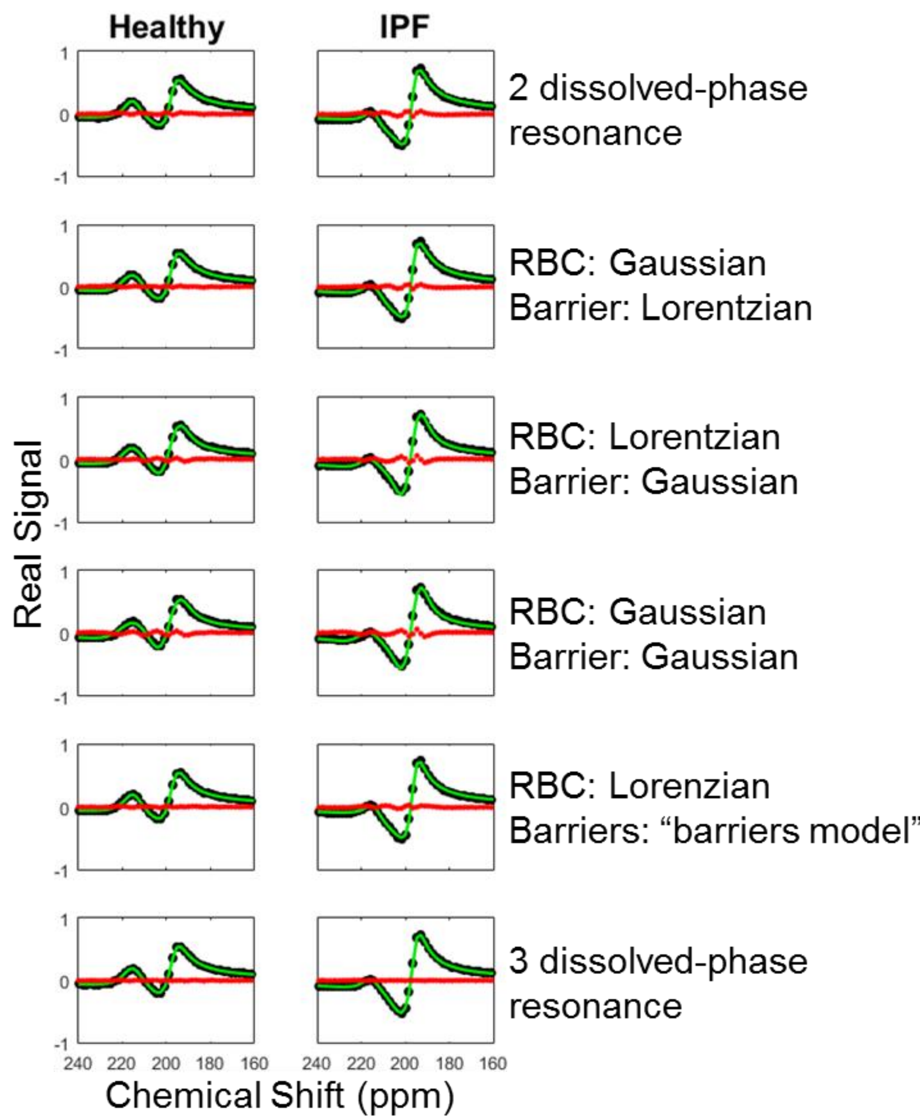

Figure 23. The real component of measured data (black dots), fits (green line), and residual errors (red dots) for a representative healthy and IPF subjects.

The healthy volunteer has low and unpatterned residual error when a Lorentzian is used for both the RBC and barrier resonance. Visually, the error does not increase when the RBC resonance is fit to a Gaussian peak, or the barrier peak it fit to the barriers model. Patterned residual error appears when the barrier is fit to a Gaussian model, regardless of the assumed RBC lineshape.

In the IPF spectrum, obvious patterned residual error is present under the two dissolved-phase peaks. As expected, this error is removed when an additional dissolved-phase resonance is added. When only the barrier peak, or both the barrier and RBC peak are fit to a Gaussian instead of a Lorentzian the residual error increases and remains patterned. The residual error slightly decreases when the RBC resonance is assumed to have a Gaussian lineshape while the barrier is Lorentzian. The two-dissolved phase model that exhibits the lowest error is the barriers model.

For each subject, all of the models were ordered from greatest residual error (most error) to lowest residual error (least error). The number of times a model had a certain rank is found in Figure 4a.

The models that assumed the signal contained two dissolved-phase peaks that were either Lorentzian or Gaussian had the most error. Consistent with Figure 3, models that included a Gaussian barrier resonance had the highest error. GG exhibited the greatest residual error for every healthy volunteer and 9 out of the 12 subjects with IPF. The model with the highest error for the remaining 3 subjects with IPF was LL. Out of the four Lorentzian/Gaussian lineshape combinations, GL had the lowest residual error most often and provided a higher quality fit, from the perspective of residual error, than the traditional model with two Lorentzian peaks.

It is not surprising the three dissolved-phase model had the lowest error for every subject. The additional peak increases the number of fit parameters and due to the properties of least square optimization the total error must decrease.

The barriers model had the next lowest residual error for all of the subjects, and the lowest error of all of the two dissolved-phase fits. On average, the barriers model had a 9.6% reduction in error compared to GL, but was 1.7 times higher than LLL.

Figure 24b displays of the magnitude of the residual error for every subject. The similarity in the mean value of the total error between models is indicative of the variability from subject to subject. The model with three dissolved-phases had the least variability in residual error between subjects, 0.94 ± 0.30. The mean and standard deviation of the two peaks fits were all very similar and ranged from 1.58 – 2.24 ± 0.76 - 1.04.

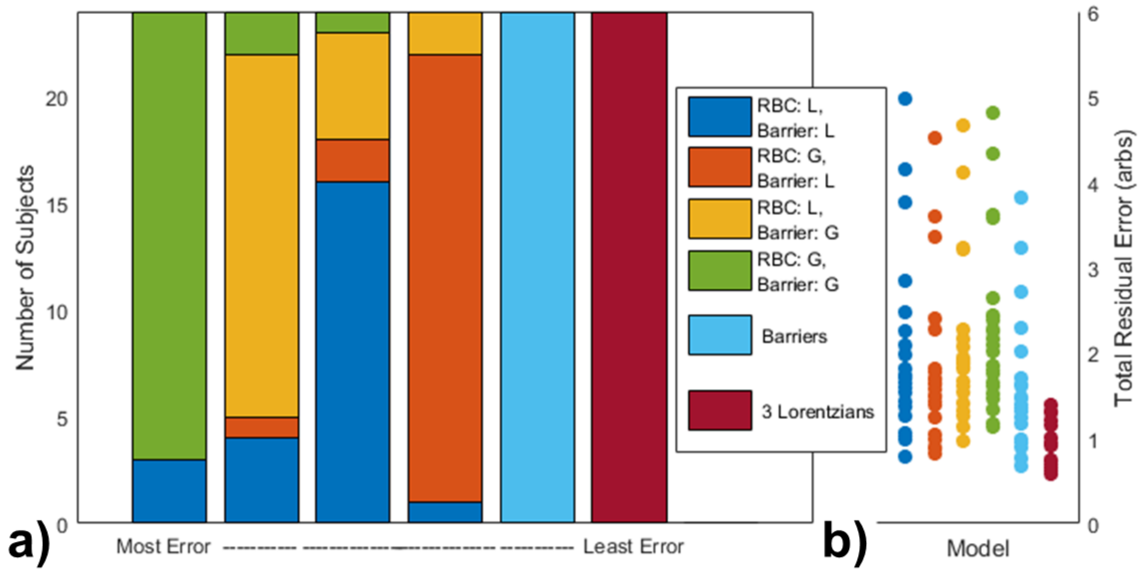

Figure 24. (a) When the performance of the 6 different fitting models is compared, the two-dissolved phase fit with the lowest residual error is the barriers model. (b) The magnitude of the total residual error has a wide variation over the 24 subjects.

5.2.2 RBC Chemical Shift

The RBC chemical shift for each model was reported separately for healthy and IPF cohorts and is displayed in Figure 25. The two subjects with IPF that had chemical shifts low enough to be considered statistical outliers in the LL model were also outliers in the GL and barriers models. However, in the LG and GG models they exhibited the two highest chemical shifts.

Using the traditional two Lorentzian peak fit, the difference between healthy volunteers and subjects with IPF was 3.15 ppm ($P < 0.001$). This difference was reduced to 0.63 ppm ($P = 0.05$) when an additional independent Lorentzian was incorporated in the model (LLL). The reduction in separation is attributable to the large increase of the

RBC chemical shift of subjects with IPF, 2.96 ppm, with only a slight increase for healthy volunteers, 0.44 ppm. Across all of the models, the mean RBC chemical shift for healthy volunteers was relatively stable with a range of 1.55 ppm. Conversely, for subjects with IPF, the models presented much greater variability in the RBC chemical shift with a range of 5.68 ppm.

In the majority of models, healthy volunteers had a greater chemical shift than patients with IPF. However, when the barrier peak was assumed to have a Gaussian lineshape the relationship was inverted and the average chemical shift for subjects with IPF was 0.90 (LG,P = 0.07) and 1.48 ppm (GG, P = 0.014) greater than healthy volunteers. The only model that did not exhibit a statistically significant difference between the two cohorts was LG.

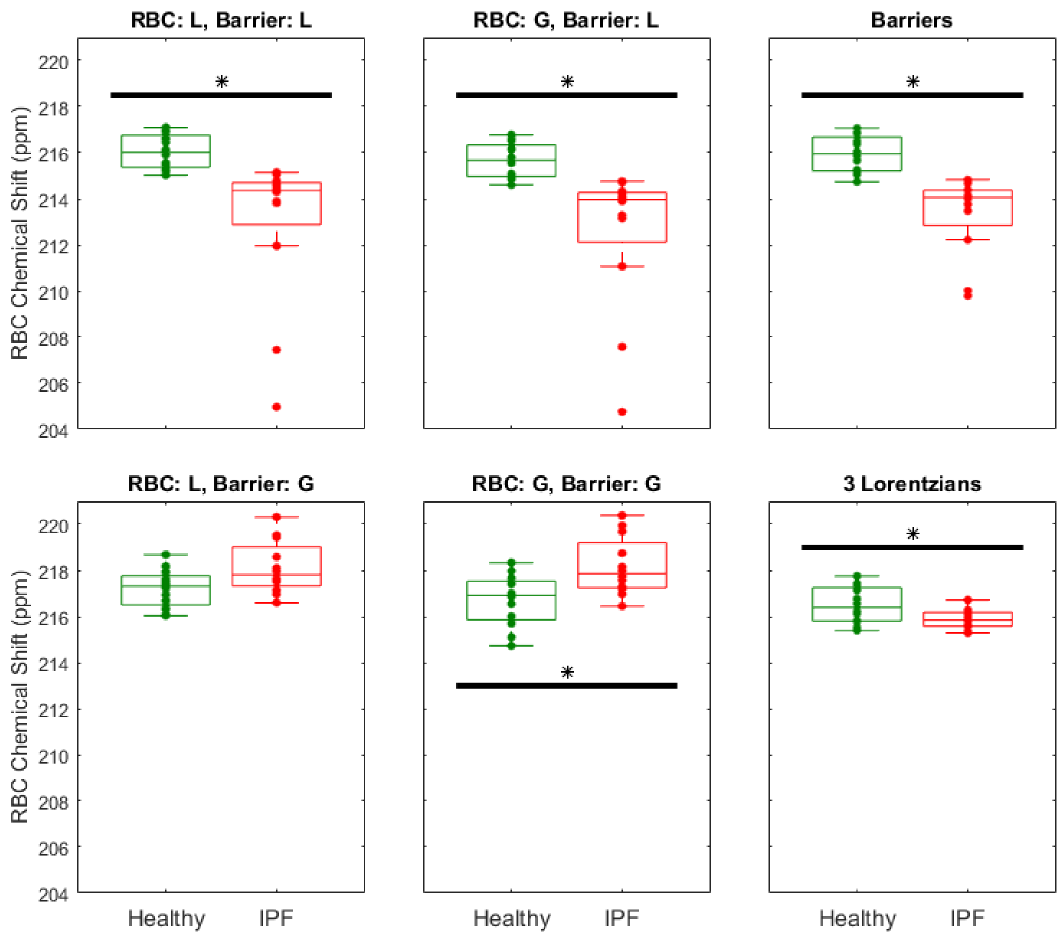

Figure 25. Comparing the RBC chemical shift of different fitting models among healthy volunteers (green) and subjects with IPF (red). * denotes statistical difference between groups (*P* < 0.05).

5.3 Discussion

The two most common lineshapes used in ^{129}Xe spectroscopy are the Lorentzian and the Gaussian. A Lorentzian peak models a monoexpoential function in the time domain and represents the intrinsic decay of ^{129}Xe. However, the measured signal is never purely Lorentzian due to a spread of resonant frequencies caused by imperfect shimming and susceptibility variations. Most often peaks are assigned their lineshape based on which model provides the lower residual error. In reality, measured lineshapes are neither Lorentzian nor Gaussian. For ^{129}Xe spectra acquired during calibration, a combination of a Gaussian RBC and Lorentzian barrier was found to have the lowest residual error out of all of the Gaussian/Lorentizian combinations.

The large bulk susceptibility difference between air and tissue causes severe line broadening in the ^{129}Xe dissolved-phase spectrum making it very hard to fit the ^{129}Xe signal to normal spectral peaks. Some previous studies recognized the deviation of the peak shapes from Lorentzians or Gaussians and chose to integrate numerically [43, 55]. In proton MRI, there is known to be inhomogeneous line broadening of the spectral peak of an inflated lung [68, 69]. Therefore, it is reasonable to investigate the possibility that one of the peaks in the three dissolved-phase fit is not truly a separate peak, but rather inhomogeneous line broadening. This was simulated by the barriers fit, which consistently had the lowest residual error out of all of the two-dissolved phase fits.

In addition to evaluating the quality of the fits using residual error, the fits can also be examined to ensure that they return chemical shifts within known physiological ranges. Extensive in vitro studies have characterized the relationship between blood oxygenation level and the RBC chemical shift and report a 5.5 ppm increase in the RBC chemical shift as blood oxygenation increases from 0 to 1 [41, 42]. Subjects with IPF have impaired gas exchange and lower sO_2 than a healthy volunteer, and subsequently they should have a lower RBC chemical shift. For that reason, the two models that fit the barrier resonance to a Gaussian are most likely a bad representation of the physiological system because they return RBC chemical shifts that are higher for subjects with IPF than healthy volunteers.

The models can also be assessed by the range of reported RBC chemical shifts with a maximum theoretical value of 5.5. The only model that meets this limit is the 3 dissolved-phase model. Nevertheless, the models do exhibit a difference in the relative range of RBC chemical shifts. The LL and GL models contain two chemical shift values that are below 210 ppm. Since the average RBC chemical shift is approximately 215 ppm, the absolute lowest RBC shift based on blood oxygenation is 209.5 ppm. Even though the lower RBC chemical shifts are outliers, the measurements are still valid and ideally should be within the limits set by oxygenation levels. These extremely low values suggest that these models are incorrectly estimating RBC chemical shift and are not accurately modeling the spectral structure. Although the barriers model still contains RBC chemical shifts below 210 ppm, the two outlying values are closer to the physiological cut-off.

5.3.1 Barriers Fitting in Dynamic Spectroscopy

Out of all of the two dissolved-phase models the barrier fit had the lowest residual error and the RBC chemical shift range that best matched with theoretical values. To test the ability of the barrier model to describe the dynamic ^{129}Xe, a subset of dynamic data from subjects with IPF were re-fit using a barriers model. Figure 26 displays the change in spectral parameters over time for a barriers fit for the IPF subject shown in Section 3.2.2. The dependent peak parameters in theses fits were derived by averaging the breath hold FIDs together and fitting to three dissolved-phase resonances. Compared to the three dissolved-phase resonance model shown in Section 3.4.1, the spectral parameters in the barriers model appear less noisy. However, much like the three dissolve-phase fit, the RBC chemical shift and phase oscillations are smaller and appear to have the same amplitude as a healthy volunteer.

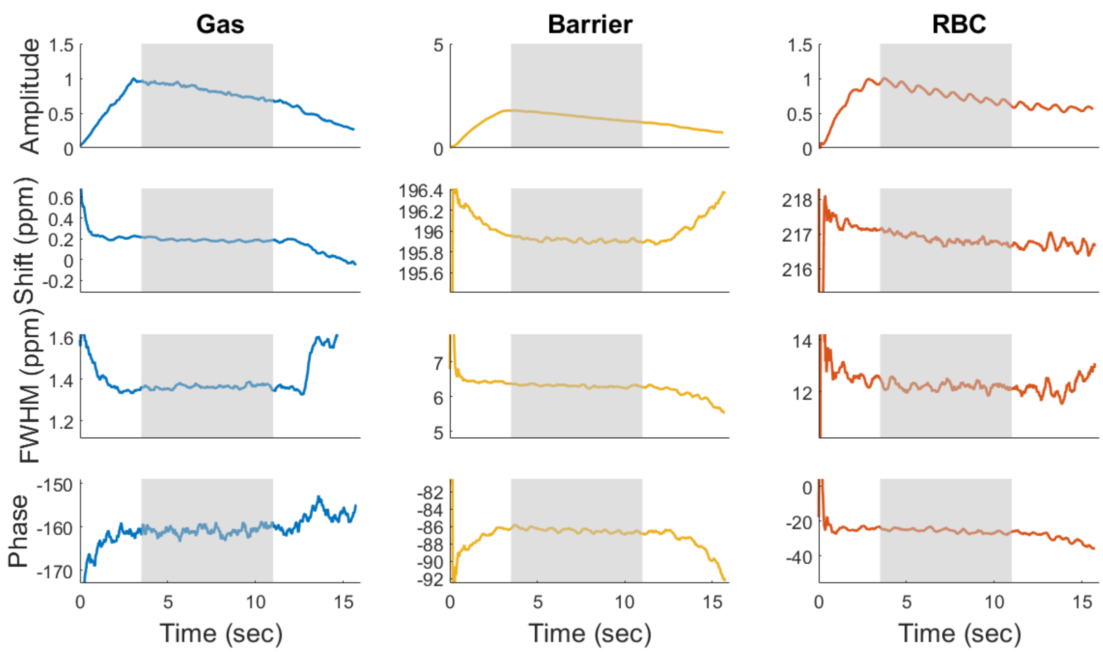

Figure 26. Temporal changes in the spectroscopic parameters of ^{129}Xe for a subject with IPF when a barriers model is used for fitting in an subject with IPF. There are no notable oscillations in the RBC chemical shift or phase.

6 Conclusion

^{129}Xe MRI is already recognized as a method imaging pulmonary function by imaging the density of ^{129}Xe in the airspaces, barrier tissue, and RBCs. However, imaging alone does not have the capability of probing the physiological changes that are the root cause of decreased lung function. ^{129}Xe spectroscopy probes the underlying physiology and is a valuable noninvasive tool for evaluating lung function. Here, we examined the temporal dynamics of spectroscopic parameters in healthy volunteers and subjects with IPF throughout a simple breathing maneuver. We found that breathing maneuver was reflected in the chemical shift and line width of the ^{129}Xe RBC, barrier, and gas resonances. Additionally, we observed that the RBC spectral parameters oscillated at the cardiac pulsation frequency for all subjects. However, in IPF subjects the peak-to-peak change in the RBC chemical shift and phase was three times higher than in healthy volunteers. Due to the relationship between RBC chemical shift and blood oxygenation, dynamic spectroscopy has the potential to measure oxygenation changes on the timescale of the cardiac cycle.

A digital dynamic spectroscopy phantom was created to examine the effect of various spectroscopic models on the analysis methods. We found that the analysis slightly underestimates peak-to-peak changes, most likely due to the use of a boxcar filter. However, it might be possible to correct measured peak-to-peak changes to account for the temporal averaging from the filter. We also used this phantom to demonstrate that the large oscillations in the RBC chemical shift and phase of subjects with IPF are not simply the result of improper signal decomposition.

A lineshape analysis was performed to determine if the ^{129}Xe spectra were better fit to non-Lorentizan peak shapes. We concluded that the residual error of the fit could be reduced by fitting the barrier resonance to a linear combination of a dependent and an independent Lorentzian. When this model was applied to the dynamic spectroscopy, the large RBC chemical shift and phase oscillations were present in some, but not all of the subjects with IPF.

Despite not discovering an exact mathematical model for fitting ^{129}Xe spectroscopy, there is still a difference between the temporal dynamics of the underlying spectral structure between healthy volunteers and subjects with IPF. The temporal dynamics of ^{129}Xe spectroscopy have the potential to be used a biomarker for disease progression and help distinguish between various pathologies.

6.1 Future Work

The current problem that is paramount to proper analysis of ^{129}Xe dynamic spectroscopy is characterizing the ^{129}Xe spectral structure. Currently, ^{129}Xe dissolved-phase spectra are fit to either two or three Lorentzian resonance. When a model with two resonances is used, clean and regular oscillations are present in the RBC chemical shift and phase of subjects with IPF. However, these oscillations almost completely disappear when the spectra are fit to a three-resonance system. Many spectral structures were simulated using the dynamic spectroscopy digital phantom, but none of them exhibited the same characteristics as the in vivo data. This suggests that we do not currently have a model that accurately represents the ^{129}Xe spectral structure.

One of the challenges in analyzing ^{129}Xe spectroscopy is decomposing the dissolved-phase resonances with relatively low spectral resolution (3.46 ppm and 1.78 ppm). While we cannot sacrifice SNR to increase spectral resolution, we can use a higher external magnetic field to increase the frequency shift between peaks, which subsequently enhances spectral resolution. Recently, our group transitioned from a 1.5 T to a 3 T scanner. We are excited to apply our analysis techniques to new spectroscopic data acquired at 3 T in hopes that the improved spectral resolution will help us determine the best model for fitting the ^{129}Xe spectra in the human lung.

References

1. Kochanek, K.D., et al., *Mortality in the united states, 2013.* NCHS data brief, 2014. **178**(178): p. 1-8.

2. Bhattacharya, S., et al., *Molecular biomarkers for quantitative and discrete COPD phenotypes.* American journal of respiratory cell and molecular biology, 2009. **40**(3): p. 359-367.

3. Kim, H.Y., R.H. DeKruyff, and D.T. Umetsu, *The many paths to asthma: phenotype shaped by innate and adaptive immunity.* Nature immunology, 2010. **11**(7): p. 577-584.

4. Jahani, N., et al., *Assessment of regional ventilation and deformation using 4D-CT imaging for healthy human lungs during tidal breathing.* Journal of Applied Physiology, 2015. **119**(10): p. 1064-1074.

5. Sodickson, A., et al., *Recurrent CT, cumulative radiation exposure, and associated radiation-induced cancer risks from CT of adults 1.* Radiology, 2009. **251**(1): p. 175-184.

6. Petersson, J., et al., *Regional lung blood flow and ventilation in upright humans studied with quantitative SPECT.* Respiratory physiology & neurobiology, 2009. **166**(1): p. 54-60.

7. Rhodes, C., et al., *Quantification of regional V/Q ratios in humans by use of PET. I. Theory.* Journal of Applied Physiology, 1989. **66**(4): p. 1896-1904.

8. Levin, D.L., M.L. Schiebler, and S.R. Hopkins, *Physiology for the pulmonary functional imager.* European Journal of Radiology, 2017. **86**: p. 308-312.

9. Chen, R., et al., *Tissue-blood partition coefficient for xenon: temperature and hematocrit dependence.* Journal of Applied Physiology, 1980. **49**(2): p. 178-183.

10. Kaushik, S.S., et al., *Measuring diffusion limitation with a perfusion-limited gas—hyperpolarized 129Xe gas-transfer spectroscopy in patients with idiopathic pulmonary fibrosis.* Journal of Applied Physiology, 2014. **117**(6): p. 577-585.

11. Wang, Z., et al., *Quantitative analysis of hyperpolarized ^{129}Xe Gas Transfer MRI.* Medical Physics, in press.

12. Robertson, S.H., et al. *^{129}Xe pulmonary gas exchange spectroscopy in idiopathic pulonary fibrosis*. in *ISMRM 24th Annual Meeting*. 2016. Singapore.

13. Kaushik, S.S., et al., *Single-breath clinical imaging of hyperpolarized 129xe in the airspaces, barrier, and red blood cells using an interleaved 3D radial 1-point Dixon acquisition.* Magnetic Resonance in Medicine, 2016. **75**(4): p. 1434-1443.

14. Walker, T.G. and W. Happer, *Spin-exchange optical pumping of noble-gas nuclei.* Reviews of Modern Physics, 1997. **69**(2): p. 629.

15. Appelt, S., et al., *Theory of spin-exchange optical pumping of 3 He and 129 Xe.* Physical Review A, 1998. **58**(2): p. 1412.

16. Happer, W., *Optical pumping.* Reviews of Modern Physics, 1972. **44**(2): p. 169.

17. Happer, W. and W. Van Wijngaarden, *An optical pumping primer.* Hyperfine Interactions, 1987. **38**(1): p. 435-470.

18. Kadlecek, S., *Magnetic Resonance Imaging with Polarized Gases: Although conventional MRI cannot track inhaled or dissolved gases in the body, physicians may soon be able to do so using specially prepared atoms.* American scientist, 2002. **90**(6): p. 540-549.

19. Möller, H.E., et al., *MRI of the lungs using hyperpolarized noble gases.* Magnetic Resonance in Medicine, 2002. **47**(6): p. 1029-1051.

20. Bouchiat, M.A., T. Carver, and C. Varnum, *Nuclear polarization in He 3 gas induced by optical pumping and dipolar exchange.* Physical Review Letters, 1960. **5**(8): p. 373.

21. Driehuys, B., et al., *High-volume production of laser-polarized 129Xe.* Applied Physics Letters, 1996. **69**(12): p. 1668-1670.

22. McDonough, J.E., et al., *Small-airway obstruction and emphysema in chronic obstructive pulmonary disease.* New England Journal of Medicine, 2011. **365**(17): p. 1567-1575.

23. Raghu, G., et al., *Incidence and prevalence of idiopathic pulmonary fibrosis.* American journal of respiratory and critical care medicine, 2006. **174**(7): p. 810-816.

24. King, T.E., A. Pardo, and M. Selman, *Idiopathic pulmonary fibrosis.* The Lancet, 2011. **378**(9807): p. 1949-1961.

25. Selman, M., T.E. King, and A. Pardo, *Idiopathic pulmonary fibrosis: prevailing and evolving hypotheses about its pathogenesis and implications for therapy.* Annals of internal medicine, 2001. **134**(2): p. 136-151.

26. Kreider, M.E., et al., *Complications of video-assisted thoracoscopic lung biopsy in patients with interstitial lung disease.* The Annals of thoracic surgery, 2007. **83**(3): p. 1140-1144.

27. Lettieri, C.J., et al., *Outcomes and safety of surgical lung biopsy for interstitial lung disease.* CHEST Journal, 2005. **127**(5): p. 1600-1605.

28. Collard, H.R., et al., *Changes in clinical and physiologic variables predict survival in idiopathic pulmonary fibrosis.* American journal of respiratory and critical care medicine, 2003. **168**(5): p. 538-542.

29. King Jr, T.E., et al., *A phase 3 trial of pirfenidone in patients with idiopathic pulmonary fibrosis.* N Engl J Med, 2014. **2014**(370): p. 2083-2092.

30. Richeldi, L., et al., *Efficacy and safety of nintedanib in idiopathic pulmonary fibrosis.* New England Journal of Medicine, 2014. **370**(22): p. 2071-2082.

31. Albert, M., et al., *Biological magnetic resonance imaging using laser-polarized 129Xe.* 1994.

32. Mugler, J.P., et al., *MR imaging and spectroscopy using hyperpolarized 129Xe gas: preliminary human results.* Magnetic resonance in medicine, 1997. **37**(6): p. 809-815.

33. Swanson, S.D., et al., *Distribution and dynamics of laser-polarized 129 Xe magnetization in vivo.* 1999.

34. Wagshul, M.E., et al., *In vivo MR imaging and spectroscopy using hyperpolarized 129Xe.* Magnetic resonance in medicine, 1996. **36**(2): p. 183-191.

35. Cleveland, Z.I., et al., *Hyperpolarized 129 Xe MR imaging of alveolar gas uptake in humans.* PloS one, 2010. **5**(8): p. e12192.

36. Driehuys, B., et al., *Imaging alveolar–capillary gas transfer using hyperpolarized 129Xe MRI.* Proceedings of the National Academy of Sciences, 2006. **103**(48): p. 18278-18283.

37. Mugler, J.P., et al., *Simultaneous magnetic resonance imaging of ventilation distribution and gas uptake in the human lung using hyperpolarized xenon-129.* Proceedings of the National Academy of Sciences, 2010. **107**(50): p. 21707-21712.

38. Patz, S., et al., *Human pulmonary imaging and spectroscopy with hyperpolarized 129 Xe at 0.2 T.* Academic radiology, 2008. **15**(6): p. 713-727.

39. Ruppert, K., et al., *Probing lung physiology with xenon polarization transfer contrast (XTC).* Magnetic Resonance in Medicine, 2000. **44**(3): p. 349-357.

40. Ruppert, K., et al., *Exploring lung function with hyperpolarized 129Xe nuclear magnetic resonance.* Magnetic resonance in medicine, 2004. **51**(4): p. 676-687.

41. Norquay, G., et al., *129Xe chemical shift in human blood and pulmonary blood oxygenation measurement in humans using hyperpolarized 129Xe NMR.* Magnetic resonance in medicine, 2016.

42. Wolber, J., et al., *Hyperpolarized 129Xe NMR as a probe for blood oxygenation.* Magnetic resonance in medicine, 2000. **43**(4): p. 491-496.

43. Ruppert, K., et al., *Detecting pulmonary capillary blood pulsations using hyperpolarized xenon-129 chemical shift saturation recovery (CSSR) MR spectroscopy.* Magnetic resonance in medicine, 2015.

44. Limes, M., et al., *Robust solid Xe 129 longitudinal relaxation times.* Physical Review B, 2016. **94**(9): p. 094309.

45. He, M., et al., *Dose and pulse sequence considerations for hyperpolarized 129 Xe ventilation MRI.* Magnetic resonance imaging, 2015. **33**(7): p. 877-885.

46. Weathersby, P. and L. Homer, *Solubility of inert gases in biological fluids and tissues: a review.* Undersea biomedical research, 1980. **7**(4): p. 277-296.

47. Hoult, D.I., *Sensitivity and power deposition in a high-field imaging experiment.* Journal of Magnetic Resonance Imaging, 2000. **12**(1): p. 46-67.

48. Doyle, M., et al., *SIFT, a postprocessing method that increases the signal-to-noise ratio of spectra which vary in time.* Journal of Magnetic Resonance, Series B, 1994. **103**(2): p. 128-133.

49. Rowland, B., et al., *Spectral improvement by fourier thresholding of in vivo dynamic spectroscopy data.* Magnetic resonance in medicine, 2015.

50. Robertson, S.H., et al., *Uncovering a third dissolved-phase 129Xe resonance in the human lung: Quantifying spectroscopic features in healthy subjects and patients with idiopathic pulmonary fibrosis.* Magnetic resonance in medicine, 2016.

51. Montigny, F., J. Brondeau, and D. Canet, *Analysis of time-domain NMR data by standard non-linear least-squares.* Chemical Physics Letters, 1990. **170**(2-3): p. 175-180.

52. Coleman, T.F. and Y. Li, *An interior trust region approach for nonlinear minimization subject to bounds.* SIAM Journal on optimization, 1996. **6**(2): p. 418-445.

53. Jameson, C.J., A.K. Jameson, and S.M. Cohen, *Temperature and density dependence of 129Xe chemical shift in xenon gas.* The Journal of Chemical Physics, 1973. **59**(8): p. 4540-4546.

54. Virgincar, R.S., et al., *Establishing an accurate gas phase reference frequency to quantify 129Xe chemical shifts in vivo.* Magnetic Resonance in Medicine, 2017. **77**(4): p. 1438-1445.

55. Qing, K., et al., *Assessment of lung function in asthma and COPD using hyperpolarized 129Xe chemical shift saturation recovery spectroscopy and dissolved-phase MRI.* NMR in biomedicine, 2014. **27**(12): p. 1490-1501.

56. Chen, X.J., et al., *Spatially resolved measurements of hyperpolarized gas properties in the lung in vivo. Part I: diffusion coefficient.* Magnetic resonance in medicine, 1999. **42**(4): p. 721-728.

57. Fichele, S., et al., *MRI of helium-3 gas in healthy lungs: posture related variations of alveolar size.* Journal of Magnetic Resonance Imaging, 2004. **20**(2): p. 331-335.

58. Glazier, J., et al., *Vertical gradient of alveolar size in lungs of dogs frozen intact.* Journal of Applied Physiology, 1967. **23**(5): p. 694-705.

59. Hajari, A.J., et al., *Morphometric changes in the human pulmonary acinus during inflation.* Journal of Applied Physiology, 2012. **112**(6): p. 937-943.

60. Glazier, J., et al., *Measurements of capillary dimensions and blood volume in rapidly frozen lungs.* Journal of Applied Physiology, 1969. **26**(1): p. 65-76.

61. Tsunoda, S., et al., *Lung volume, thickness of alveolar walls, and microscopic anisotropy of expansion.* Respiration physiology, 1974. **22**(3): p. 285-296.

62. Hughes, J.M.B., et al., *Effect of lung volume on the distribution of pulmonary blood flow in man.* Respiration Physiology, 1968. **4**(1): p. 58-72.

63. Topulos, G.P., et al., *Fractional changes in lung capillary blood volume and oxygen saturation during the cardiac cycle in rabbits.* Journal of Applied Physiology, 1997. **82**(5): p. 1668-1676.

64. Albrecht, K., et al., *The Fahraeus effect in narrow capillaries (id 3.3 to 11.0 μm).* Microvascular research, 1979. **18**(1): p. 33-47.

65. Barbee, J.H. and G.R. Cokelet, *The fahraeus effect.* Microvascular research, 1971. **3**(1): p. 6-16.

66. West, J.B., *Respiratory physiology: the essentials*. 2012: Lippincott Williams & Wilkins.

67. Brudin, L., et al., *Regional lung hematocrit in humans using positron emission tomography*. Journal of Applied Physiology, 1986. **60**(4): p. 1155-1163.

68. Bertolina, J., et al., *Experimental verification of inhomogeneous line-broadening calculations in lung models and other inhomogeneous structures.* Journal of Magnetic Resonance (1969), 1992. **99**(1): p. 161-169.

69. Cutillo, A.G., et al., *Alveolar air-tissue interface and nuclear magnetic resonance behavior of lung.* Journal of Applied Physiology, 1991. **70**(5): p. 2145-2154.